

Review

Magnetic Nanoparticle-Based High-Performance Positive and Negative Magnetic Resonance Imaging Contrast Agents

Tirsew Tegafaw ¹, Shuwen Liu ¹, Mohammad Yaseen Ahmad ¹, Abdullah Khamis Ali Al Saidi ¹,
Dejun Zhao ¹, Ying Liu ¹, Sung-Wook Nam ², Yongmin Chang ^{2,*} and Gang Ho Lee ^{1,*}

¹ Department of Chemistry, College of Natural Sciences, Kyungpook National University, Taegu 41566, Republic of Korea; tegafawtirsew@yahoo.com (T.T.); liushuwen0701@gmail.com (S.L.); yaseen.knu@gmail.com (M.Y.A.); abdullah_al_saidi@hotmail.com (A.K.A.A.S.); djzhao.chem@gmail.com (D.Z.); ly1124161@gmail.com (Y.L.)

² Department of Molecular Medicine, School of Medicine, Kyungpook National University, Taegu 41944, Republic of Korea; nams@knu.ac.kr

* Correspondence: ychang@knu.ac.kr (Y.C.); ghlee@mail.knu.ac.kr (G.H.L.)

Abstract: In recent decades, magnetic nanoparticles (MNPs) have attracted considerable research interest as versatile substances for various biomedical applications, particularly as contrast agents in magnetic resonance imaging (MRI). Depending on their composition and particle size, most MNPs are either paramagnetic or superparamagnetic. The unique, advanced magnetic properties of MNPs, such as appreciable paramagnetic or strong superparamagnetic moments at room temperature, along with their large surface area, easy surface functionalization, and the ability to offer stronger contrast enhancements in MRI, make them superior to molecular MRI contrast agents. As a result, MNPs are promising candidates for various diagnostic and therapeutic applications. They can function as either positive (T_1) or negative (T_2) MRI contrast agents, producing brighter or darker MR images, respectively. In addition, they can function as dual-modal T_1 and T_2 MRI contrast agents, producing either brighter or darker MR images, depending on the operational mode. It is essential that the MNPs are grafted with hydrophilic and biocompatible ligands to maintain their nontoxicity and colloidal stability in aqueous media. The colloidal stability of MNPs is critical in order to achieve a high-performance MRI function. Most of the MNP-based MRI contrast agents reported in the literature are still in the developmental stage. With continuous progress being made in the detailed scientific research on them, their use in clinical settings may be realized in the future. In this study, we present an overview of the recent developments in the various types of MNP-based MRI contrast agents and their in vivo applications.

Keywords: magnetic nanoparticle; magnetic resonance imaging; contrast agent; high-performance



Citation: Tegafaw, T.; Liu, S.; Ahmad, M.Y.; Saidi, A.K.A.A.; Zhao, D.; Liu, Y.; Nam, S.-W.; Chang, Y.; Lee, G.H. Magnetic Nanoparticle-Based High-Performance Positive and Negative Magnetic Resonance Imaging Contrast Agents. *Pharmaceutics* **2023**, *15*, 1745. <https://doi.org/10.3390/pharmaceutics15061745>

Academic Editor: Axel Zeitler

Received: 27 May 2023

Revised: 13 June 2023

Accepted: 14 June 2023

Published: 15 June 2023



Copyright: © 2023 by the authors. Licensee MDPI, Basel, Switzerland. This article is an open access article distributed under the terms and conditions of the Creative Commons Attribution (CC BY) license (<https://creativecommons.org/licenses/by/4.0/>).

1. Introduction

Magnetic resonance imaging (MRI) is a widely used, advanced and effective diagnostic imaging technique owing to its distinct advantages over other imaging modalities [1–4]. Its unique features include high spatial resolution [5,6], excellent soft-tissue contrast [7–9], lack of ionizing radiation risk [10,11], and high imaging depths. Owing to these factors, MRI is often the preferred choice for diagnosing various medical conditions, particularly in pregnant women and children who may be sensitive to ionizing radiation [10,12,13]. This is because MRI is operated under low-energy radiofrequency radiation in contrast to invasive X-ray computed tomography (CT) and positron emission tomography (PET) scans which use high-energy ionizing radiation and can damage cells and tissues, causing side effects. Although MRI supports high spatial resolution (0.05–0.5 mm) [5], its sensitivity is relatively low [5] because of the inherently small population difference between two proton spin energy states in nuclear magnetic resonance, making the detection of small biological events, such as early-stage small lesions, difficult. However, MRI sensitivity can

be improved using MRI contrast agents because they accelerate proton spin relaxation and enhance proton signals [14,15]. Various MRI contrast agents have been investigated and developed to achieve this goal [16–20]. Importantly, their accumulation in the region of interest (ROI) compared to surrounding tissues generates image contrast between the ROI and surrounding tissues, allowing for sensitive detection and diagnosis of the ROI.

MRI contrast agents do not produce signals but rather enhance the sensitivity and resolution of MRI via MR signal and contrast enhancements. Preclinical and clinical studies have investigated various types of MRI contrast agents [16–20], including Gd chelates such as Magnevist, Dotarem, Omniscan, and ProHance [21,22], which are currently being clinically developed as T₁ MRI contrast agents. Other agents that have been extensively investigated include Mn chelates, Gd-based nanoparticles (NPs), Mn-based NPs, and superparamagnetic iron oxide nanoparticles (SPIONs). In addition, paramagnetic lanthanide (Ln)-based NPs (Ln = Dy, Ho, and Tb) have drawn interest as potential T₂ MRI contrast agents in high MR fields owing to their appreciable paramagnetic moments at room temperature [23–28]. Molecular MRI contrast agents such as Gd chelates and Mn chelates typically have low longitudinal (r₁) and transverse (r₂) proton spin relaxivity and short blood circulation times owing to their rapid renal excretion, thus necessitating large amounts of injection doses to achieve their detection level. These requirements can increase the risk of biotoxicity because of the potential liberation of free metal ions in the body. For instance, free Gd³⁺ ions can cause nephrogenic systemic fibrosis (NSF) in patients with kidney diseases, resulting in the thickening and darkening of the skin and the reduction of organ function in the heart and lungs [22,29,30]. In addition, recent studies indicated that clinically developed Gd chelates could be deposited in the brain after repeated use and cause neurotoxicity [31,32]. SPION-based MRI contrast agents are more biocompatible than other metal-based NP contrast agents because iron is consumed in the human body as an essential element [33]; for example, iron is a central element in hemoglobin for oxygen binding. Among MNPs, only Fe-based NPs have been commercialized. In the past, Feridex, Sinerem, and Resovist, which are dextran-coated SPIONs, were approved by the Food and Drug Administration (FDA), USA for clinical trials in liver (Feridex and Resovist) and lymph node (Sinerem) imaging via intravenous injection [34–38]. In addition, Lumirem was approved by the FDA for gastrointestinal imaging via oral administration [34]. However, safety concerns led to Feridex's and Sinerem's withdrawal from the market because of back pain [36]. Lumirem was withdrawn from the market due to little use, but not for safety concerns [34]. Currently, only Resovist is allowed for liver imaging in limited countries [36–38].

Compared with metal chelates, magnetic NP (MNP)-based MRI contrast agents have numerous advantages. Not only do they have stronger magnetic moments and longer blood circulation times, resulting in higher contrast in images, but also support multifunctional applications such as multimodal imaging and the therapy of diseases via surface functionalization and drug delivery [39]. These advantages make them superior to molecular agents. Among the MNPs studied, SPIONs and Gd-based NPs have been most intensively investigated over the past decade owing to their outstanding magnetic properties over other MNPs. Notably, Gd-based NPs have higher r₁ values than commercial Gd chelates [40–45]. Recently, researchers have explored paramagnetic NPs made of Dy, Ho, and Tb as potential alternatives to SPIONs as T₂ MRI contrast agents at high MR fields (>3 T) because of their high r₂ values. As the paramagnetic moments of these NPs increase with increasing MR field, they become comparable to those of SPIONs [23–28].

MNPs are composed of two parts: a magnetic core that enhances MR signals and a surface-coating ligand layer that ensures colloidal stability and nontoxicity. High colloidal stability in aqueous media is necessary for obtaining high-performance MRI function and maximal MR signal enhancement. Otherwise, the precipitation of MNPs can result in a reduced interaction between MNPs and water proton spins, resulting in reduced MR signal enhancement. In this review, we focused on newly developed, MNP-based MRI contrast agents and their in vivo applications. The review includes MNPs made of Gd, Mn, Fe,

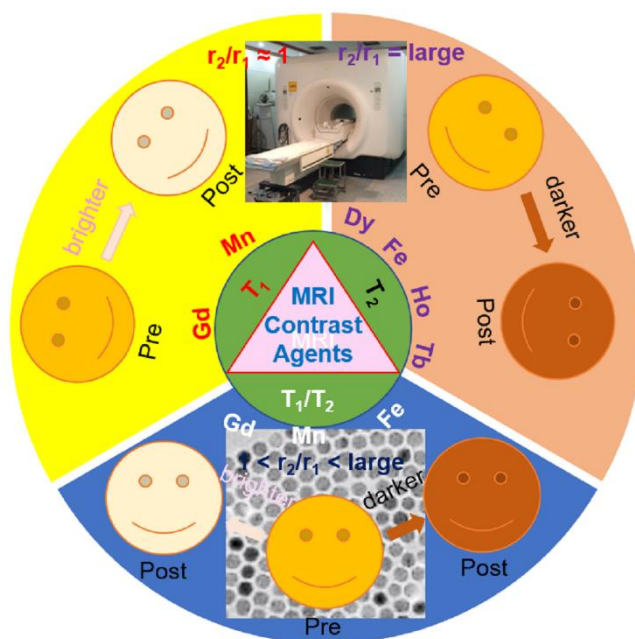
Dy, Ho, and Tb, which function as T_1 MRI contrast agents; T_2 MRI contrast agents; or dual-modal T_1 and T_2 MRI contrast agents.

2. The Principle of Imaging Mode (T_1 or T_2 or Both)

The effectiveness of MNPs as MRI contrast agents depends on their r_1 and r_2 values, and their r_2/r_1 ratios [46,47]. As the longitudinal (T_1) proton spin relaxation always occurs with the transverse (T_2) proton spin relaxation, but not the other way around, the ideal T_1 MRI contrast agent should have high r_1 values and r_2/r_1 ratios close to 1.0. In contrast, the ideal T_2 MRI contrast agent should have high r_2 values and high r_2/r_1 ratios to solely induce T_2 proton spin relaxation [46,47]. Dual-modal T_1 and T_2 MRI contrast agents should have both high r_1 and r_2 values, with r_2/r_1 ratios between those of ideal T_1 and ideal T_2 MRI contrast agents. The primary parameter that affects r_1 and r_2 values and r_2/r_1 ratios is the MNP composition. The particle size and surface-coating ligand are also important. The types of imaging modes possible with MNPs are summarized in Table 1 and Scheme 1.

Table 1. Classification of imaging modes of MNPs (++: a major application; +: a minor application).

Imaging Mode	Fe-Based MNP	Mn-Based MNP	Gd-Based MNP	Dy-Based MNP	Ho-Based MNP	Tb-Based MNP
T_1	+	++	++			
T_2	++	+	+	++	++	++
Dual-modal T_1 and T_2	+	+	+			



Scheme 1. Types of imaging modes possible with MNPs made of Gd, Mn, Fe, Dy, Ho, and Tb.

2.1. T_1 Imaging Mode

The longitudinal (T_1) proton spin relaxation primarily depends on metal ion spin layers present on the MNP surfaces, which interact with nearby proton spins, accelerating T_1 proton spin relaxation along the z-axis (the so-called inner sphere model [48–50]). Therefore, MNPs made of Gd^{3+} ($s = 7/2$), Mn^{2+} ($s = 5/2$), and Fe^{3+} ($s = 5/2$) can contribute to T_1 proton spin relaxation because their slow s-electrons closely match with slow proton spin relaxation [48]. Gd^{3+} strongly induces T_1 proton spin relaxation because of its highest electron spin magnetic moment ($s = 7/2$) among the periodic table elements [51]. Conversely, fast electrons with orbital angular moment components do not match with slow

proton spin relaxation and thus negligibly induce T_1 proton spin relaxation [48], resulting in negligible r_1 values. For example, MNPs made of Ln^{3+} ($\text{Ln} = \text{Dy}, \text{Ho}, \text{and Tb}$) negligibly induce T_1 proton spin relaxation because of their 4f-electrons with orbital angular momentum components [23–28].

Recent studies indicate that the particle diameter of Fe-based NPs is critical in achieving optimal T_1 proton spin relaxation because smaller NPs offer greater surface exposure of Fe^{3+} to the surrounding water protons [52–58]. Park and co-workers reported that the optimal particle diameter range of Gd-based NPs for maximal T_1 proton spin relaxation or the maximal r_1 value is 1–2.5 nm [40]. They proposed the cooperative effects of surface Gd^{3+} in accelerating T_1 proton spin relaxation to explain this.

2.2. T_2 Imaging Mode

MNPs become magnetized upon exposure to an external magnetic field, resulting in local magnetic field fluctuations around the MNPs because of their thermal motion in solution [59–61]. The local magnetic field fluctuations accelerate the transverse (T_2) proton spin relaxation (so-called outer sphere model [48–50]), which corresponds to the dephasing of proton spin magnetic moments along the xy plane. MNPs with high magnetic moments, such as SPIONs, can generate high local magnetic field fluctuations that induce strong T_2 proton spin relaxation, resulting in high r_2 values. Note that MNPs made of Dy, Ho, and Tb exhibit appreciable paramagnetic moments at room temperature and thus exhibit appreciable r_2 values [23–28,62–64]. They solely induce T_2 proton spin relaxation, resulting in negligible r_1 values. Notably, these paramagnetic moments increase with increasing MR field, resulting in even higher r_2 values than those of SPIONs at very high MR fields [62].

2.3. T_1 and T_2 Dual-Imaging Mode

Conventional MRI contrast agents can serve as either T_1 or T_2 MRI contrast agents. However, the introduction of T_1 and T_2 dual-modal MRI contrast agents has enabled more accurate diagnosis of disease via complementary T_1 and T_2 MR images [65–71]. Dual-modal MR images can be easily obtained by changing the operational mode of the same MRI scanner, unlike other dual-modal imaging techniques (such as MRI-CT, CT-PET, and MRI-PET) that require a combination of two different imaging machines that are expensive, inconvenient, and time-consuming.

Designing dual-modal MNPs requires careful synthetic strategies to ensure they function in a dual-mode. The composition, particle diameter, and surface-coating ligand of MNPs can be controlled to optimize the r_1 and r_2 values [65,72–76]. For instance, small and hydrophilic surface-coating ligands can attract water molecules close to the MNPs, resulting in high r_1 and r_2 values, whereas large and hydrophobic surface-coating ligands do not, resulting in small r_1 and r_2 values [72,73,76]. Larger MNPs can provide higher r_2 values and higher r_2/r_1 ratios owing to their enhanced magnetic moments and reduced amounts of surface metal ions and thus are more suitable as T_2 MRI contrast agents [74]. The composition of MNPs may be controlled to obtain r_1 and r_2 values suitable for dual-modal imaging [65].

3. Examples of MNP-Based MRI Contrast Agents

3.1. T_1 MRI Contrast Agents

3.1.1. Gd-Based NPs

Among MNPs, Gd-based NPs possess the most suitable relaxivity properties for T_1 MRI contrast agents, owing to Gd^{3+} having the highest spin magnetic moment ($s = 7/2$) among the elements in the periodic table. The r_1 values of Gd-based NPs are higher than those [48,50] of Gd chelates because of the high density of Gd^{3+} per NP, making them high-performance T_1 MRI contrast agents. Among various types of Gd-based NPs, such as Gd_2O_3 , GdF_3 , and NaGdF_4 NPs, the Gd_2O_3 NPs have been most intensively investigated thus far.

Park et al. synthesized D-glucuronic acid-coated Gd_2O_3 NPs (mean particle diameter = 1 nm) in polyol solvent [40]. The transmission electron microscope (TEM) image is presented in Figure 1a(i). The synthesized NPs exhibited a high r_1 value of $9.9 \text{ s}^{-1}\text{mM}^{-1}$ and thus high positive T_1 contrasts in mouse brain tumors after intravenous injection at 1.5 T (Figure 1a(ii)).

Recently, Yang et al. reported polyvinylpyrrolidone (PVP)-coated Gd_2O_3 NPs (PVP Mw = 10,000 amu and mean particle diameter = 2.5 ± 0.8 nm) with a high r_1 value of $10.8 \text{ mM}^{-1}\text{s}^{-1}$ at 3 T [77]. Appreciable contrasts in T_1 MR images of the tumor, kidney, bladder, and liver were observed after intravenous injection at 3 T.

Dai et al. reported a comparison study between polyethylene glycol (PEG)-coated (or PEGylated)- Gd_2O_3 NPs (PEG Mw = 600 amu and mean hydrodynamic diameter = 36.35 nm) and commercially available Magnevist (or gadopentetic acid) [78]. The PEGylated- Gd_2O_3 NPs exhibited a higher r_1 value of $29.0 \text{ mM}^{-1}\text{s}^{-1}$ than that ($= 4.2 \text{ mM}^{-1}\text{s}^{-1}$) of Magnevist at 3 T. The T_1 MR images of tumor-bearing mice were obtained 3 T (Figure 1b). The contrast enhancement of PEGylated- Gd_2O_3 NPs in the tumor was stronger than that of Magnevist at the same injection dose, confirming the superiority of PEGylated- Gd_2O_3 NPs, compared with Magnevist.

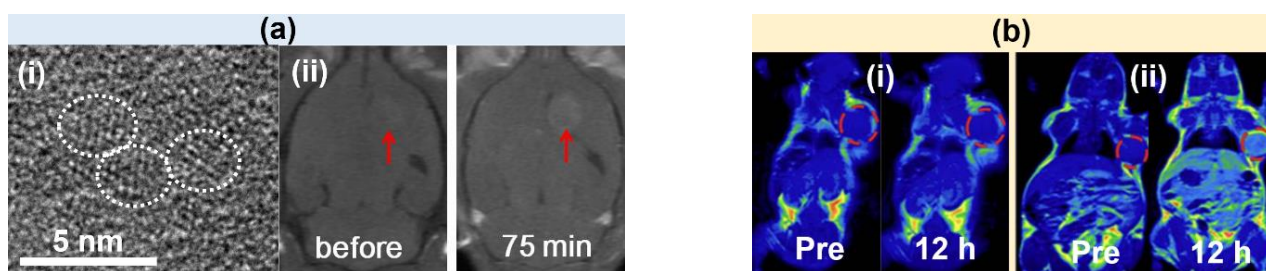


Figure 1. (a) (i) TEM image of D-glucuronic acid-coated Gd_2O_3 NPs (labeled as dotted circles) and (ii) in vivo T_1 MR images of mouse brain tumor (labeled with arrows) before and 75 min after intravenous injection at 1.5 T [40]. (b) In vivo T_1 MR images of mice bearing renal carcinoma tumor (labeled with red circles), before (labeled as “Pre”) and 12 h after intravenous injection of (i) Magnevist and (ii) PEG- Gd_2O_3 NPs at 3 T [78].

3.1.2. Mn-Based NPs

Mn-based NPs have emerged as alternatives to Gd-based NPs because of their lower toxicity. Mn-based NPs have shown appreciable paramagnetic moments at room temperature owing to Mn^{2+} ($s = 5/2$), but their paramagnetic moments are lower than those of Gd-based NPs because Mn^{2+} ($s = 5/2$) has a lower spin magnetic moment than Gd^{3+} ($s = 7/2$).

Wei et al. synthesized zwitterionic dopamine sulfonate (ZDS)-coated ultrasmall MnO NPs (simply, USMnO@ZDS) (mean particle diameter = 1.1 nm), which exhibited a high r_1 value of $15.6 \pm 0.4 \text{ mM}^{-1}\text{s}^{-1}$ and a high r_2 value of $26.9 \pm 1.1 \text{ mM}^{-1}\text{s}^{-1}$ at 0.5 T [79]. The TEM image of USMnO@ZDS is presented in Figure 2a(i). The USMnO@ZDS exhibited positive contrast enhancements in mouse brains after intravenous injection at 9.4 T, while *meso*-2,3-dimercaptosuccinic acid (DMSA)-grafted MnO NPs (simply, USMnO@DMSA) did not (Figure 2a(ii)). This indicated that the surface modification of MnO NPs with proper ligands such as ZDS, not DMSA, is crucial for the penetration of the NPs through the brain–blood barrier.

Li et al. synthesized PEG-coated MnO NPs (PEG Mw = 600 amu and mean particle diameter = 1.9 nm), with a high r_1 value of $12.942 \text{ s}^{-1}\text{mM}^{-1}$ and an r_2/r_1 ratio of 4.66 at 3 T [80]. They conjugated the PEG-MnO NPs with AS1411 aptamer to target tumors, resulting in AS1411-PEG-MnO NPs that retained contrast in the tumor for up to 7 days after intravenous injection. However, the contrast provided by PEG-MnO NPs disappeared after 1 day of injection because of their lack of tumor targeting.

Xiao et al. prepared ligand-free Mn_3O_4 NPs (mean particle diameter = 9 nm) using laser ablation in aqueous media [81], as shown in a TEM image presented in Figure 2b(i). These uncoated Mn_3O_4 NPs had an r_1 value of $8.26 \text{ mM}^{-1}\text{s}^{-1}$ at 3 T, which did not significantly affect the cell viability, owing to their low toxicity. T_1 MR images at 3 T revealed high positive contrast enhancements in the xenografted tumor 30 min after intravenous injection (Figure 2b(ii)), demonstrating their potential as a T_1 MRI contrast agent.

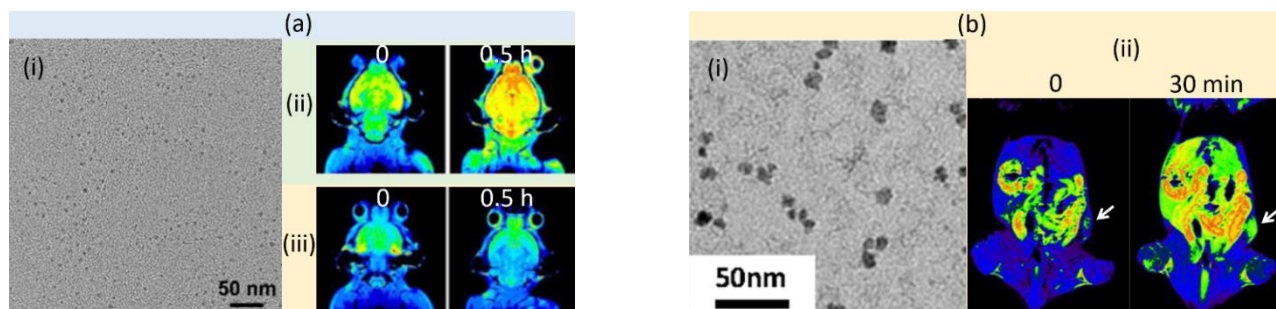


Figure 2. (a) (i) TEM image of USMnO@ZDS NPs and in vivo T_1 MR images of mouse brains, before (labeled as “0”) and 0.5 h after intravenous injection of (ii) USMnO@ZDS and (iii) USMnO@DMSA at 9.4 T [79]. (b) (i) TEM image of uncoated Mn_3O_4 NPs and (ii) T_1 MR images of Balb/c nude mice bearing a nasopharyngeal carcinoma xenografted tumor (indicated with white arrows), before (labeled as “0”) and 30 min after intravenous injection of Mn_3O_4 NPs at 3 T [81].

3.2. T_2 MRI Contrast Agents

3.2.1. Fe-Based NPs

Because of the high magnetic moments and better biocompatibility of Fe-based NPs compared with other metal-based NPs, they have been extensively investigated as T_2 MRI contrast agents.

Zhao et al. highlighted the importance of size and morphology tuning for the development of SPIONs with high r_2 values [82]. Octapod NPs showed higher r_2 values than spherical NPs, with r_2 values of 679.25 ± 30 , 209.03 ± 15 , 125.86 ± 9 , and 59.91 ± 6 $30 \text{ mM}^{-1}\text{s}^{-1}$ at 7 T for octapod-30 (mean edge length = 30 nm), octapod-20 (mean edge length = 20 nm), spherical-16 (mean particle diameter = 16 nm), and spherical-10 NPs (mean particle diameter = 10 nm), respectively. The TEM images of octapod-30 and spherical-16 NPs are presented in Figure 3a(i,ii) respectively. In vivo results at 7 T demonstrated that octapod-30 NPs produced higher MR contrasts in the tumor than those of spherical-16 NPs (Figure 3a(iii,iv)).

Wang et al. reported the one-pot synthesis of ultrasmall SPIONs (uBSPIOs) using bovine serum albumin as a scaffold [83]. The resulting uBSPIOs (mean particle diameter = $4.78 \pm 0.55 \text{ nm}$) exhibited a high r_2 value of $444.56 \pm 8.82 \text{ mM}^{-1}\text{s}^{-1}$ at 7 T. These uBSPIOs provided high negative contrasts in the T_2 MR images of the tumor. In addition, the uBSPIOs demonstrated no cytotoxicity in vitro and negligible organ toxicity in vivo.

Leal et al. synthesized PEGylated SPIONs (mean particle diameter = 6 nm) with PEG molecular weight (MW) ranging from 600 to 8000 amu [84]. The PEG3000-SPIONs (PEG Mw = 3000 amu) exhibited better in vivo performance, with longer circulation times and slower liver uptake than other MW PEG-coated SPIONs. This was because high MW PEGs (6000–8000 amu) led to NP aggregations, whereas low MW PEGs (≤ 1500 amu) could not stabilize the NPs in physiological media. The PEG1500-, PEG3000-, PEG6000- and PEG8000-SPIONs had r_2 values of 90, 103, 190, and 180 $\text{mM}^{-1}\text{s}^{-1}$ at 1.5 T and the r_2 values of 114, 151, 253, and 254 $\text{mM}^{-1}\text{s}^{-1}$ at 9.4 T, respectively. After intravenous injection into mice tails at 9.4 T, the PEGylated SPIONs exhibited negative contrast enhancements in T_2 MR images, demonstrating their potential as T_2 MRI contrast agents.

Lee et al. synthesized ferrimagnetic iron oxide nanocubes (FIONs) (mean edge length = 22 nm, as presented in a TEM image in Figure 3b(i)) and encapsulated them in PEG-phospholipids to obtain water-dispersible FIONs (WFIONs) [85]. The WFIONs exhibited an

extremely high r_2 value of $761 \text{ mM}^{-1}\text{s}^{-1}$ at 3 T, which is close to the theoretically predicted maximum r_2 value of $\sim 800 \text{ mM}^{-1}\text{s}^{-1}$ for 22 nm sized NPs with a saturation magnetization of 106 emu/g. Notably, their study demonstrated that FION aggregates could generate a very strong magnetic field that caused nearby water proton spins to completely lose their phase, leading to a decrease in their r_2 value as the NP size increased. In vivo MR images revealed a distinct signal decrease in the tumor site 1 h after intravenous injection (Figure 3b(ii)).

Maurea et al. reported the clinical applications of a commercial T_2 MRI contrast agent Resovist in humans [38]. Resovist is carboxydextrane-coated SPION with a hydrodynamic diameter ranging from 45 to 60 nm and r_2 and r_1 values of 151.0 and $25.4 \text{ mM}^{-1}\text{s}^{-1}$, respectively [35]. As shown in Figure 3c, hepatocellular carcinoma could be more clearly observed after intravenous injection compared with no injection (labeled as before) [38].

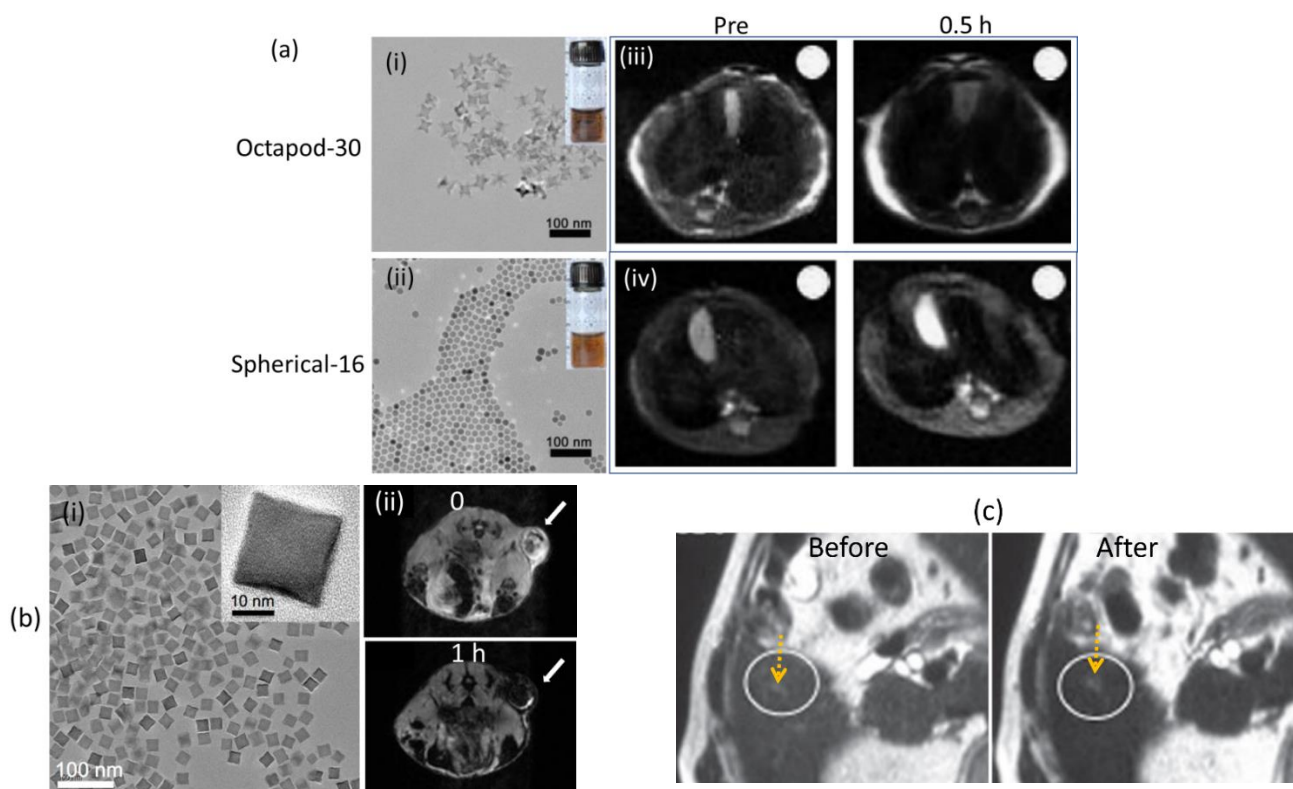


Figure 3. (a) TEM images of (i) octapod-30 and (ii) spherical-16 NPs (scale bars are 100 nm). T_2 MR images in mouse livers at 7 T before (or Pre) and 0.5 h after intravenous injection of (iii) octapod-30 and (iv) spherical-16 NPs (the white dot is the signal reference using water in an NMR tube) [82]. (b) (i) TEM image of FIONs and (ii) in vivo T_2 MR images of the tumor site at 3 T before (or 0) and 1 h after intravenous injection of WFIONs (arrows indicate the tumor sites) [85]. (c) A small (5 mm) hepatocellular carcinoma (indicated with arrows) proven by biopsy. T_2 MR images at 1.5 T before and after intravenous injection of Resovist into patients showing clearer faint focal hyperintensity after injection in the hepatic segment [38].

3.2.2. Dy-Based NPs

Dy-based NPs have gained significant interest as a new class of T_2 MRI contrast agents because of their appreciable paramagnetic moments at room temperature. Dy has the highest effective magnetic moment (μ_{eff}) ($10.65 \mu_B$) among the elements in the periodic table [51]. Currently, most MRI contrast agents are operated at clinical MR fields (1.5–3 T). However, Dy-based NPs can become more powerful at higher MR fields such as 7 and 9.4 T because their paramagnetic moment increases with the increasing MR field. This will trigger a new opportunity to generate powerful T_2 MRI contrast agents suitable for high-field MRI scanners. In addition to T_2 relaxation by outer sphere model, Curie-spin relaxation is

also important for Dy-based NPs [86,87]. This is because T_2 relaxation is induced by the modulated magnetic dipolar interaction between proton spins and thermally averaged electronic spins (or Curie-spins) of Dy^{3+} in NPs by NP motion. This Curie-spin relaxation becomes important in high MR fields.

González-Mancebo et al. synthesized rhombus-like DyF_3 NPs (mean length \times width = 110×50 nm) in ethylene glycol, which served as the solvent and surface-coating ligand [88]. The DyF_3 NPs exhibited a remarkably high r_2 value of $380.4 \text{ mM}^{-1}\text{s}^{-1}$ at 9.4 T, with a high r_2/r_1 ratio of 559.37, demonstrating their potential as highly effective T_2 MRI contrast agents.

Kattel et al. reported on the effectiveness of D-glucuronic acid-coated Dy_2O_3 NPs and $Dy(OH)_3$ nanorods as T_2 MRI contrast agents [89]. The D-glucuronic acid-coated Dy_2O_3 NPs (mean particle diameter = 3.2 nm) and $Dy(OH)_3$ nanorods (mean diameter \times length = 20×300 nm) exhibited negligible r_1 values and high r_2 values of 65.04 and $181.57 \text{ s}^{-1}\text{mM}^{-1}$ at 1.5 T, respectively. Dy_2O_3 NPs and $Dy(OH)_3$ nanorods also produced clear negative contrast enhancements of T_2 MR images of mouse liver and kidneys at 3 T after intravenous injection.

Recently, Yue et al. synthesized hydrophilic, nearly nontoxic, amorphous carbon-coated Dy_2O_3 NPs (mean particle diameter = 3.0 nm, as presented in a TEM image in Figure 4a(i)) [90]. The carbon coating was achieved through dextrose polymerization on the Dy_2O_3 NP surfaces, which left hydroxyl groups on the NP surfaces and made the amorphous carbon-coated Dy_2O_3 NPs colloiddally stable in aqueous media and nearly nontoxic. The amorphous carbon-coated NPs had r_1 and r_2 values of 0.1 and $5.7 \text{ s}^{-1}\text{mM}^{-1}$ at 3 T, respectively, with an r_2/r_1 ratio of 57. In vivo T_2 MR images of mouse kidneys at 3 T exhibited negative contrasts after intravenous injection, demonstrating their potential as T_2 MRI contrast agents (Figure 4a(ii)). In addition, the NPs exhibited broad photofluorescence at 490 nm (400–600 nm) upon excitation at 370 nm due to the fluorescent nature of the amorphous carbon-coating layers on the NP surfaces. Therefore, amorphous carbon-coated Dy_2O_3 NPs are suitable as dual-modal T_2 MRI-fluorescence imaging (FI) agents.

Marasini et al. developed colloiddally stable poly(acrylic acid) (PAA)-coated Dy_2O_3 NPs (PAA Mw = 1800 amu and mean particle diameter = 1.7 nm, as presented in a TEM image in Figure 4b(i)) using a simple polyol synthesis [91]. The r_1 value was negligible, but the r_2 value increased with increasing MR field such that it was $2.01 \text{ s}^{-1}\text{mM}^{-1}$ at 3 T and $11.31 \text{ s}^{-1}\text{mM}^{-1}$ at 9.4 T. In vivo T_2 MR images at 3 T exhibited clear negative contrast enhancements in mouse livers after intravenous injection (Figure 4b(ii)), demonstrating their potential as a T_2 MRI contrast agent.

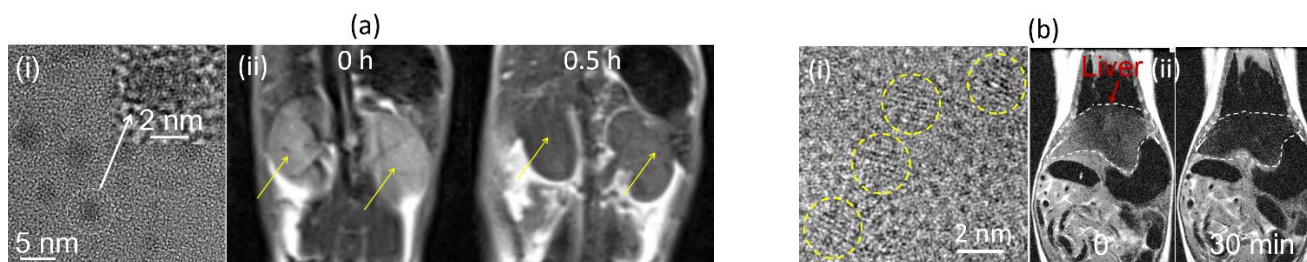


Figure 4. (a) (i) TEM image of amorphous carbon-coated Dy_2O_3 NPs and (ii) T_2 MR images in mouse kidneys (labeled with arrows) before (or 0 h) and 0.5 h after intravenous injection of amorphous carbon-coated Dy_2O_3 NPs at 3 T [90]. (b) (i) TEM image of PAA-coated Dy_2O_3 NPs (labeled with yellow circles) and (ii) T_2 MR images of mouse liver (labeled with dotted lines and an arrow) before (or 0) and 30 min after intravenous injection of PAA-coated Dy_2O_3 NPs into mice tails at 3 T [91].

Recently, Gómez-González et al. synthesized PAA-coated $DyPO_4$ NPs (PAA Mw = 1800 amu) with tunable particle diameters ranging from 23 to 57 nm using a homogeneous precipitation method in butanol [92]. They found that the r_2 values were 395, 432,

and $516 \text{ mM}^{-1}\text{s}^{-1}$ for 23, 37, and 57 nm NPs at 9.4 T, respectively. These high r_2 values confirmed the suitability of PAA-coated DyPO_4 NPs as T_2 MRI contrast agents.

3.2.3. Ho-Based NPs

Ho-based NPs exhibit appreciable paramagnetic moments at room temperature, similar to Dy-based NPs, owing to Ho with high μ_{eff} of $10.60 \mu_{\text{B}}$, the second highest value among elements in the periodic table [51]. Consequently, they are potential candidates for T_2 MRI contrast agents at high MR fields similar to Dy-based NPs.

Gómez-González et al. synthesized cube-shaped HoPO_4 NPs that were grafted with PAA ($M_w = 1800$ amu) to investigate the relationship between r_2 value and MR field (1.44 and 9.4 T) and between r_2 value and NP diameter (27, 48, and 80 nm) [93]. The r_2 value of HoPO_4 @PAA NPs increased with increasing NP diameter at 1.44 T, but failed for the largest NPs at 9.4 T because of their aggregation; consequently, the 48 nm NPs exhibited the highest r_2 value of $489.91 \text{ mM}^{-1}\text{s}^{-1}$ at 9.4 T. In vivo studies using 48 nm HoPO_4 @PAA NPs at 9.4 T revealed that, after intravenous injection, the NPs showed distinct T_2 contrasts in both the liver and spleen, demonstrating their potential as T_2 MRI contrast agents.

Atabaev et al. reported an r_2 value of $23.47 \text{ mM}^{-1}\text{s}^{-1}$ at 1.5 T for PEG-coated Ho_2O_3 NPs (PEG $M_n = 4000$ amu) with a particle diameter of 67–81 nm [94], which is high enough to be used as T_2 MRI contrast agents.

González-Mancebo et al. investigated the r_2 values of HoF_3 NPs at 9.4 T as a function of particle size and composition [88]. They synthesized two different types of HoF_3 NPs in ethylene glycol, which served as the solvent and surface-coating ligand; ellipsoid-like HoF_3 NPs (HoF-el) (mean length \times width = 70×30 nm) and rhombus-like HoF_3 NPs (HoF-rh) (mean length \times width = 110×50 nm). The NPs exhibited r_2 values of $349.98 \text{ mM}^{-1}\text{s}^{-1}$ and $608.4 \text{ mM}^{-1}\text{s}^{-1}$ at 9.4 T for HoF-el and HoF-rh, respectively. The increase in r_2 value with increasing particle size was attributed to the higher magnetization of larger NPs than smaller ones. The high r_2 values indicated that the synthesized NPs should be useful as high-field T_2 MRI contrast agents.

Recently, Zhang et al. conducted a study on PEG- HoF_3 NPs (PEG $M_w = 4000$ amu and mean particle diameter = 38 nm) as a T_2 MRI contrast agent for cancer diagnosis [95]. The NPs had an r_2 value of $117.51 \text{ mM}^{-1}\text{s}^{-1}$ at 7 T, and 24 h after intravenous injection, negative (or darker) contrasts in T_2 MR images in the tumors of tumor-bearing mice were observed because of the accumulation of NPs in the tumor, demonstrating the potential of the NPs as a T_2 MRI contrast agent.

Marasini et al. synthesized PAA-coated Ho_2O_3 NPs (PAA $M_w = 1800$ amu and mean particle diameter = 1.7 nm) using one-pot polyol synthesis [96]. The TEM image is presented in Figure 5a(i). The NPs were nearly nontoxic and colloidally stable in aqueous media without precipitation after synthesis because of their hydrophilic and biocompatible PAA coating. The PAA-coated Ho_2O_3 NPs exhibited an appreciable r_2 value of $1.44 \text{ s}^{-1}\text{mM}^{-1}$ at 3 T and an enhanced r_2 value of $9.20 \text{ s}^{-1}\text{mM}^{-1}$ at 9.4 T. In vivo T_2 MR images of the liver and kidneys exhibited strong negative contrast enhancements at 3 T, and stronger negative contrast enhancements at 9.4 T, confirming the effectiveness of the NPs as T_2 MRI contrast agents at high-MR fields (Figure 5a(ii)).

Liu et al. synthesized polyethylenimine (PEI)-coated Ho_2O_3 NPs using a one pot polyol method (PEI $M_n = 1200$ and $60,000$ amu) and investigated their potential as T_2 MRI contrast agents [97]. The NPs exhibited mean particle diameters of 2.05 and 1.90 nm and appreciable r_2 values of 13.1 and $9.9 \text{ s}^{-1}\text{mM}^{-1}$ for the PEI1200 and PEI60000-coated NPs, respectively. The same authors synthesized Ho_2O_3 NPs grafted with PEG diacid (PEGD)250 ($M_w = 250$ amu), PEGD600 ($M_w = 600$ amu), and PAA1800 ($M_w = 1800$ amu) using the one-pot polyol method (mean particle diameter = 2.1, 2.1, and 1.7 nm, respectively) [98]. The r_2 value decreased with increasing ligand-size such that $30.39 \text{ s}^{-1}\text{mM}^{-1}$ (PEGD250) $<$ $11.33 \text{ s}^{-1}\text{mM}^{-1}$ (PEGD600) $<$ $1.44 \text{ s}^{-1}\text{mM}^{-1}$ (PAA1800). In vivo T_2 MRI studies were performed at 3 T using PEGD250-coated Ho_2O_3 NPs because they had the highest r_2 value among the samples. The TEM image of PEGD250-coated Ho_2O_3 NPs is

presented in Figure 5b(i), and appreciable negative contrast enhancements in the liver and kidneys were observed (Figure 5b(ii)), demonstrating their potential as T_2 MRI contrast agents.

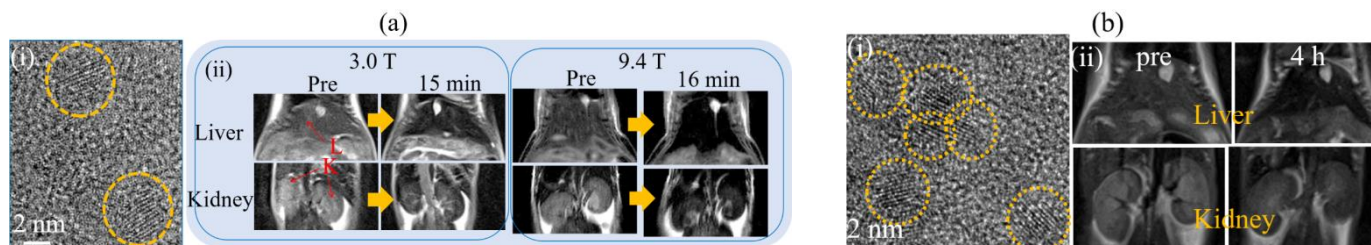


Figure 5. (a) (i) TEM image of PAA-coated Ho_2O_3 NPs (labeled with dotted circles) and (ii) in vivo T_2 MR images of mouse liver (labeled as “L”) and kidneys (labeled as “K”), before (labeled as “Pre”) and 15 or 16 min after intravenous injection of PAA-coated Ho_2O_3 NPs into mice tails at 3.0 and 9.4 T [96]. (b) (i) TEM image (labeled with dotted circles) and (ii) in vivo T_2 MR images of mouse liver and kidneys at 3 T, before (labeled as “pre”) and 4 h after intravenous injection of PEGD250-coated Ho_2O_3 NPs [98].

3.2.4. Tb-Based NPs

Tb-based NPs have shown great potential as T_2 MRI contrast agents at high MR fields owing to their appreciable paramagnetic moments at room temperature, which were similar to Dy- and Ho-based NPs because Tb has μ_{eff} of $9.72 \mu_B$ [51]. Despite their promising potential as T_2 MRI contrast agents at high MR fields, only a few studies on Tb-based NPs have been reported.

Zheng et al. synthesized PEI-coated TbF_3 NPs (PEI Mn = 25,000 amu) using a facile solvothermal method [99]. The NPs had a plate morphology (mean particle diameter \times thickness = 160×29 nm), as presented in the TEM image in Figure 6a(i). They obtained high r_2 values of 6.54 and $395.77 \text{ mM}^{-1}\text{s}^{-1}$ at 0.5 and 7 T, respectively. An in vivo T_2 MRI study at 7 T revealed that after injection into mouse tail veins, the MR signal intensities in the liver, spleen, and kidneys decreased significantly after injection, indicating the accumulation of NPs in these organs. An example of a liver MR image 15 min after injection is presented in Figure 6a(ii).

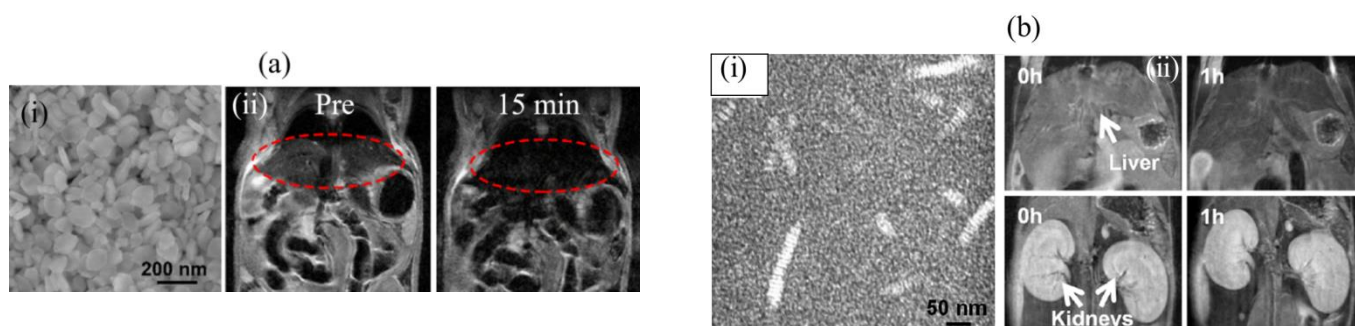


Figure 6. (a) (i) TEM image of PEI-coated TbF_3 NPs and (ii) in vivo T_2 MR images of Kunming mouse liver (labeled as dotted circles), before (labeled as “Pre”) and 15 min after intravenous injection of PEI-coated TbF_3 NPs at 7 T [99]. (b) (i) STEM image of PEG-TbNRs and (ii) in vivo T_2 MR images of mouse liver and kidneys (labeled with arrows), before (labeled as “0 h”) and 1 h after intravenous injection of the PEG-TbNRs at 9.4 T [24].

Marasini et al. synthesized D-glucuronic acid-coated Tb_2O_3 NPs (mean particle diameter = 2.0 nm) as a potential dual-modal T_2 MRI-FI agent because Tb also emits photons in the 545 nm region [100]. The D-glucuronic acid-coated NPs exhibited r_2 values of $7.68 \text{ mM}^{-1}\text{s}^{-1}$ at 1.5 T, $33.97 \text{ mM}^{-1}\text{s}^{-1}$ at 3 T, and $53.67 \text{ mM}^{-1}\text{s}^{-1}$ at 9.4 T, indicating

that they have r_2 values suitable as T_2 MRI contrast agents. Furthermore, the NPs exhibited fluorescence in the green region, making them suitable as dual-modal T_2 MRI-FI agents.

Recently, Caro et al. investigated the potential of PEG-coated Tb-based nanorods (PEG-TbNRs) as multimodal bioimaging agents [24]. The PEG-TbNRs (PEG Mw = 3000 amu and mean particle diameter \times length = 2×9 nm) exhibited high colloidal stability and excellent luminescent, magnetic, and X-ray attenuation properties. The scanning TEM (STEM) image demonstrating the nanorod morphology is presented in Figure 6b(i). The r_2 values of PEG-TbNRs at 1.44 and 9.4 T were estimated to be 10.4 and 48.5 $\text{mM}^{-1}\text{s}^{-1}$, respectively. In vivo T_2 MR images at 9.4 T exhibited appreciable negative contrast enhancements in the liver and kidneys after intravenous injection (Figure 6b(ii)), demonstrating the potential of PEG-TbNRs as T_2 MRI contrast agents.

3.3. T_1 and T_2 Dual-Modal MNPs

Despite the promising potential of dual-modal imaging compared to single-modal imaging, there are limited reports on T_1 and T_2 dual-modal contrast agents in MRI [65–71,101–112]. MNPs used for dual-modal operation should have high r_1 and r_2 values with r_2/r_1 ratios higher than 1, but not excessively high. To use Gd-based NPs as T_1 and T_2 dual-modal contrast agents, the r_2/r_1 ratios should be increased because their ratios are close to 1, while the r_2/r_1 ratios of SPIONs should be decreased because their ratios are very high. Mn-based NPs can be used as T_1 and T_2 dual-modal contrast agents because of their suitable r_2/r_1 ratios. However, Ln-based NPs (Ln = Dy, Ho, and Tb) can only be used as T_2 MRI contrast agents because they have negligible r_1 values [96–100].

Miao et al. synthesized PAA-coated Fe_3O_4 NPs (PAA = 1000 amu and mean particle diameter = 5.1 nm). The NPs exhibited r_1 and r_2 values of 10.52 and 38.97 $\text{mM}^{-1}\text{s}^{-1}$ ($r_2/r_1 = 3.70$) at 1.41 T, respectively [109]. The TEM image is presented in Figure 7a(i). The performance of the NPs as a dual-modal T_1 and T_2 MRI contrast agent was demonstrated from T_1 and T_2 MR images at 3 T, where positive contrasts were clearly observed in the rabbit vasculature (Figure 7a(ii)) and negative contrasts were clearly observed in the rabbit popliteal lymph node (dotted circle) (Figure 7a(iii)).

Li et al. developed monodispersed water-soluble and biocompatible ultrasmall magnetic iron oxide nanoparticles (mean particle diameter = 3.3 ± 0.5 nm) grafted with poly(methacrylic acid) (PMAC, $M_n = 6359$ amu) in aqueous media using a high-temperature coprecipitation method [104]. The PMAC-grafted NPs exhibited $r_1 = 8.3$ and $r_2 = 35.1 \text{ s}^{-1}\text{mM}^{-1}$ ($r_2/r_1 = 4.2$) at 4.7 T, and demonstrated their potential as dual-modal T_1 and T_2 MRI contrast agents. After intravenous injection, positive and negative contrasts were observed in the T_1 and T_2 MR images of mice liver and kidneys, respectively.

Mekuria et al. reported on the encapsulation of Gd_2O_3 NPs (diameter = 3–5 nm) with 4.5 generation (G4.5) polyamidoamine (PAMAM) dendrimers and then, conjugated them with PEG (Mp = 10,000 amu) to obtain PEG-G4.5- Gd_2O_3 NPs [110]. The PEG-G4.5- Gd_2O_3 NPs exhibited a high r_1 value of 53.9 $\text{mM}^{-1}\text{s}^{-1}$ and a high r_2 value of 182.81 $\text{mM}^{-1}\text{s}^{-1}$ ($r_2/r_1 = 3.4$) at 7 T. An in vivo T_1 MRI study showed that the PEG-G4.5- Gd_2O_3 NPs significantly enhanced signals in mouse intestines and kidneys. In addition, the T_2 MRI study demonstrated a darker contrast in the kidneys, demonstrating the potential of G4.5- Gd_2O_3 -PEG NPs as a dual-modal T_1 and T_2 MRI contrast agent.

Recently, Marasini et al. developed a dual-modal T_1 and T_2 MRI contrast agent by coating Gd_2O_3 NPs (mean particle diameter = 2 nm) with polyaspartic acid (PASP) (Mw = ~9900 amu) using the one-pot polyol method [111]. The TEM image is presented in Figure 7b(i). The synthesized NPs exhibited high r_1 and r_2 values of 19.1 and 53.7 $\text{mM}^{-1}\text{s}^{-1}$ ($r_2/r_1 = 2.8$) at 3 T, respectively. After intravenous injection of PASP-coated Gd_2O_3 NPs into the mice tails, T_1 and T_2 contrasts were observed in the T_1 and T_2 MR images of the mouse livers at 3 T, respectively (Figure 7b(ii)). This result showed that dual-modal T_1 and T_2 MRI contrast agents prepared using Gd_2O_3 NPs could be obtained by choosing the appropriate hydrophilic polymers as surface-coating ligands, such as the PASP used in this study.

Another promising candidate for dual-modal T_1 and T_2 MRI contrast agents is Mn-based NPs. Niu et al. developed manganese oxide nanocluster-loaded (diameter < 2 nm) dual-mesoporous silica spheres (Mn-DMSS; diameter = 100–200 nm, as presented in the TEM image in Figure 7c(i)) [112]. Mn-DMSSs exhibited a high r_1 value of $10.1 \text{ mM}^{-1}\text{s}^{-1}$ and a high r_2 value of $169.7 \text{ mM}^{-1}\text{s}^{-1}$ ($r_2/r_1 = 16.8$) at 3 T. An in vivo experiment on rats at 3 T demonstrated that Mn-DMSSs exhibited a 29% signal enhancement in the liver under T_1 imaging mode and a 28% signal decrease under T_2 imaging mode (Figure 7c(ii)), demonstrating the potential of Mn-DMSSs as dual-modal T_1 and T_2 MRI contrast agents.

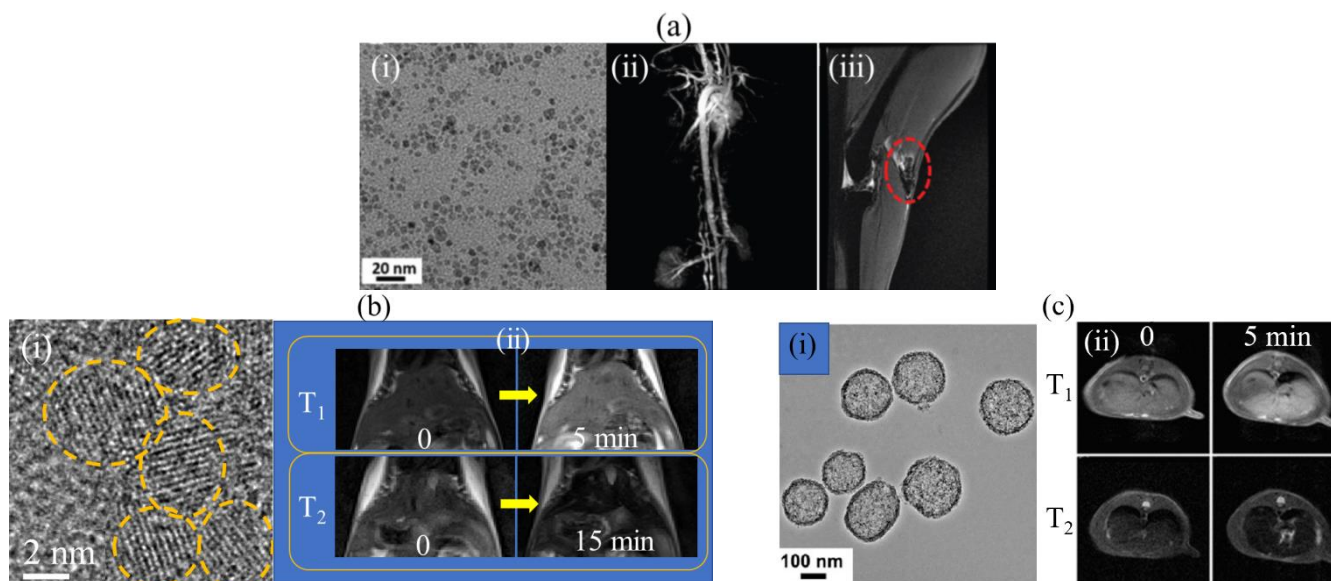


Figure 7. (a) (i) TEM image of PAA-coated Fe_3O_4 NPs (labeled with yellow circles), (ii) T_1 MR images of rabbit vasculature after intravenous injection, and (iii) T_2 MRI images of rabbit popliteal lymph node (dotted circle) after intravenous injection at 3 T [109]. (b) (i) TEM image of PASA-coated Gd_2O_3 NPs and (ii) in vivo T_1 and T_2 MR images of mouse livers, before (labeled as “0”) and 5 and 15 min after intravenous injection of PASA-coated Gd_2O_3 NPs into mice tails at 3 T [111]. (c) (i) TEM image of Mn-DMSSs and (ii) in vivo T_1 and T_2 MR images of rat livers, before (labeled as “0”) and 5 min after intravenous injection at 3 T [112].

4. Colloidal Stability, Biocompatibility, and Renal Excretion

It is essential that MNPs are coated with hydrophilic and biocompatible ligands to maintain their nontoxicity and colloidal stability in aqueous media. The colloidal stability of MNPs is critical for achieving high-performance MRI function because precipitated NPs lessen or negligibly contribute to inducing proton spin relaxation.

Compared with MNPs made of Gd, Mn, Dy, Ho, and Tb, Fe-based NPs are more biocompatible because iron is consumed in the human body as an essential element [33]; for example, it is used in hemoglobin for oxygen binding. For this reason, several Fe-based MNPs as MRI contrast agents, such as Feridex, Sinerem, and Resovist, were commercialized with approval by the FDA, USA [34–38], over other metal-based MNPs.

It is critical that MNPs should be nontoxic for biomedical applications [113,114]. Because MRI contrast agents are generally intravenously injected, it is preferred that MNPs are excreted through the renal system rather than the hepatobiliary pathway because the hepatobiliary excretion is relatively slow and MNPs could decompose during the excretion process, which would be toxic to the body. For example, free Gd^{3+} ions liberated from Gd chelates into the body could cause NSF [22,29,30]. For renal excretion, MNPs should be ultrasmall with hydrodynamic diameters less than 5 nm [115–117] because the glomerular filtration diameter in the kidneys is 4.5–5 nm [115]. It is also essential that the kinetic

stability of MNPs is high so that they do not decompose until they are excreted through the renal system as urine.

As summarized in Figure 8, MNPs as MRI contrast agents for safe, in vivo applications should be kinetically stable (i.e., no decomposition), coated with hydrophilic and biocompatible polymers for nontoxicity and colloidal stability, and ultrasmall with hydrodynamic diameters less than 5 nm for renal excretion. Under these conditions, MNPs can serve as high-performance MRI contrast agents which are superior to commercial molecular MRI contrast agents. In particular, the magnetic properties of MNPs made of Gd, Dy, Ho, and Tb are nearly size independent and thus can be made ultrasmall for renal excretion. They can strongly induce proton spin relaxation at high MR fields, implying that those MNPs are potential candidates for a new type of MRI contrast agents for high-field MRI scanners.

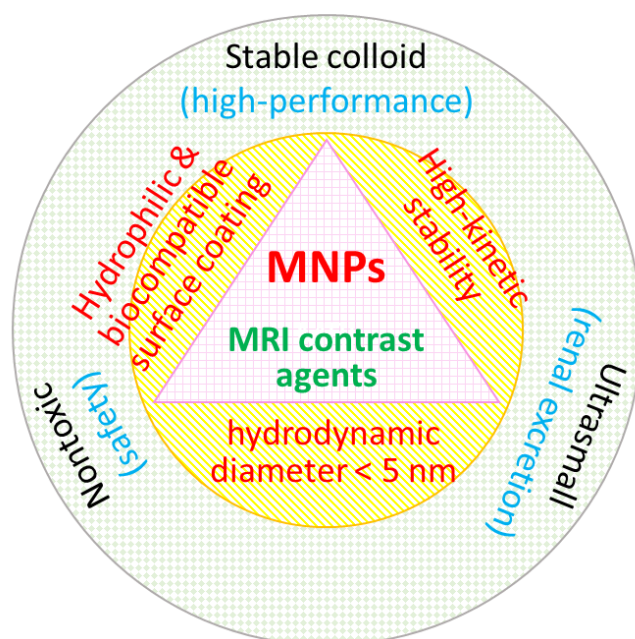


Figure 8. Conditions for MNPs for safe, in vivo application.

5. Conclusions

MRI has emerged as a promising imaging modality for accurate disease diagnosis. Although the population difference between the two proton spin energy states is small because of a small energy difference between them, the high content of hydrogens from water (~60 wt.% of the human body) and other sources in the human body results in a large number of hydrogen protons. This plays a critical role in producing MR signals and contrasts.

The MR signals and contrasts can be improved by accelerating the proton spin relaxation with MRI contrast agents. Commercial molecular MRI contrast agents such as Gd chelates typically have low r_1 and r_2 values and short blood circulation times, thus necessitating large numbers of injection doses to achieve their detection level. However, MNP-based MRI contrast agents can provide enhanced MR signals and contrast compared with those of molecular MRI contrast agents owing to their enhanced magnetic moments, high density of metals per NP, and longer blood circulation times. Moreover, MNP-based MRI contrast agents have great potential for disease therapy through drug delivery and targeting ligand conjugation on MNP surfaces. In addition, T_1 and T_2 dual-modal-imaging MNPs show great potential for improving disease diagnosis via complementary T_1 and T_2 MR images, which molecular MRI contrast agents cannot provide.

Among the MNPs, only iron oxide NPs were commercialized as T_2 MRI contrast agents, but most of them have been withdrawn from the market. Only Resovist is currently available in a few countries. Commercial T_1 MRI contrast agents are Gd chelates and

currently hold the market for all MRI contrast agents. However, they have low sensitivity owing to their low relaxivity values and short imaging times owing to their short blood circulation times. Therefore, the development of new MRI contrast agents to overcome such shortcomings is desirable. MNPs may be the breakthrough because they have high r_1 and r_2 values and long blood circulation times.

6. Perspective

This review provides an overview of MNP-based MRI contrast agents composed of Gd, Mn, Fe, Dy, Ho, and Tb. Their high-performance as MRI contrast agents was highlighted via in vivo MRI studies. However, most of MNP-based MRI contrast agents reported in the literature are still in the development stage, with limited research carried out on in vitro and early-stage in vivo small animal studies. To increase the possibility of their safe use as high-performance MRI contrast agents in clinical trials in the future, several key issues such as toxicological effects, long-term stability, and pharmacokinetics must be addressed.

Tailoring of the particle size, morphology, composition, and surface-coating ligand is essential in achieving high-performance MNP-based MRI contrast agents. Multidisciplinary collaborative research can help advance the synthetic techniques and gain an understanding of the correlation between the fundamental physicochemical properties of MNPs and their biological behaviors in vivo and in vitro. With continuous progress in detailed scientific research on MNP-based MRI contrast agents, their use in clinical settings may become feasible in the future.

Author Contributions: Conceptualization, T.T., S.L., M.Y.A., A.K.A.A.S., D.Z., Y.L., G.H.L., S.-W.N. and Y.C.; investigation, T.T., S.L., M.Y.A., A.K.A.A.S., D.Z., Y.L., G.H.L., S.-W.N. and Y.C.; writing—original draft preparation, T.T.; writing—review and editing, G.H.L. and Y.C.; funding acquisition, G.H.L., Y.C. and S.-W.N. All authors have read and agreed to the published version of the manuscript.

Funding: This work was supported by the Basic Science Research Program of the National Research Foundation (NRF) funded by the Korean government (Ministry of Science, and Information and Communications Technology: MSIT) (Basic Research Laboratory, No. 2021R1A4A1029433).

Institutional Review Board Statement: Not applicable.

Informed Consent Statement: Not applicable.

Data Availability Statement: Not applicable.

Conflicts of Interest: The authors declare no conflict of interest.

References

1. Van Beek, E.J.R.; Kuhl, C.; Anzai, Y.; Desmond, P.; Ehman, R.L.; Gong, Q.; Gold, G.; Gulani, V.; Hall-Craggs, M.; Leiner, T.; et al. Value of MRI in medicine: More than just another test? *J. Magn. Reson. Imaging* **2019**, *49*, e14–e25. [[CrossRef](#)]
2. Currie, S.; Hoggard, N.; Craven, I.J.; Hadjivassiliou, M.; Wilkinson, I.D. Understanding MRI: Basic MR physics for physicians. *Postgrad. Med. J.* **2013**, *89*, 209–223. [[CrossRef](#)]
3. Scherzinger, A.L.; Hendee, W.R. Basic Principles of Magnetic Resonance Imaging—An Update. *West. J. Med.* **1985**, *143*, 782–792.
4. Grover, V.P.B.; Tognarelli, J.M.; Crossey, M.M.E.; Cox, I.J.; Taylor-Robinson, S.D.; McPhail, M.J.W. Magnetic Resonance Imaging: Principles and Techniques: Lessons for Clinicians. *J. Clin. Exp. Hepatol.* **2015**, *5*, 246–255. [[CrossRef](#)]
5. Paeng, J.C.; Lee, D.S. Multimodal Molecular Imaging In Vivo. *Open Nucl. Med. J.* **2010**, *2*, 145–152. [[CrossRef](#)]
6. Weissleder, R.; Mahmood, U. Molecular imaging. *Radiology* **2001**, *219*, 316–333. [[CrossRef](#)]
7. Hughes, P.; Miranda, R.; Doyle, A.J. MRI imaging of soft tissue tumours of the foot and ankle. *Insights Imaging* **2019**, *10*, 60. [[CrossRef](#)] [[PubMed](#)]
8. Lee, J.H.; Kim, H.S.; Yoon, Y.C.; Seo, S.W.; Cha, M.J.; Jin, W.; Cha, J.G. Characterization of small, deeply located soft-tissue tumors: Conventional magnetic resonance imaging features and apparent diffusion coefficient for differentiation between non-malignancy and malignancy. *PLoS ONE* **2020**, *15*, e0232622. [[CrossRef](#)] [[PubMed](#)]
9. Mastrogiacomo, S.; Dou, W.; Jansen, J.A.; Walboomers, X.F. Magnetic Resonance Imaging of Hard Tissues and Hard Tissue Engineered Bio-substitutes. *Mol. Imaging. Biol.* **2019**, *21*, 1003–1019. [[CrossRef](#)] [[PubMed](#)]
10. Kellenberger, C.J.; Epelman, M.; Miller, S.F.; Babyn, P.S. Fast STIR whole-body MR imaging in children. *Radiographics* **2004**, *24*, 1317–1330. [[CrossRef](#)]
11. Yang, X.; Atalar, E. MRI-guided gene therapy. *FEBS Lett.* **2006**, *580*, 2958–2961. [[CrossRef](#)]

12. Gatta, G.; Grezia, G.D.; Cuccurullo, V.; Sardu, C.; Iovino, F.; Comune, R.; Ruggiero, A.; Chirico, M.; Forgia, D.L.; Fanizzi, A.; et al. MRI in Pregnancy and Precision Medicine: A Review from Literature. *J. Pers. Med.* **2021**, *12*, 9. [[CrossRef](#)] [[PubMed](#)]
13. Ray, J.G.; Vermeulen, M.J.; Bharatha, A.; Montanera, W.J.; Park, A.L. Association Between MRI Exposure During Pregnancy and Fetal and Childhood Outcomes. *JAMA* **2016**, *316*, 952–961. [[CrossRef](#)] [[PubMed](#)]
14. Li, Y.; Zhao, X.; Liu, X.; Cheng, K.; Han, X.; Zhang, Y.; Min, H.; Liu, G.; Xu, J.; Shi, J.; et al. A Bioinspired Nanoprobe with Multilevel Responsive T₁-Weighted MR Signal-Amplification Illuminates Ultrasmall Metastases. *Adv. Mater.* **2020**, *32*, 1906799. [[CrossRef](#)] [[PubMed](#)]
15. Lu, H.; Xu, Y.; Qiao, R.; Lu, Z.; Wang, P.; Zhang, X.; Chen, A.; Zou, L.; Wang, Z. A novel clustered SPIO nanoplatform with enhanced magnetic resonance T₂ relaxation rate for micro-tumor detection and photothermal synergistic therapy. *Nano Res.* **2020**, *13*, 2216–2225. [[CrossRef](#)]
16. Coroiu, I.; Darabont, A.; Demco, D.E. Potential contrast agents for magnetic resonance imaging. *Appl. Magn. Reson.* **1998**, *15*, 531–538. [[CrossRef](#)]
17. Geraldes, C.F.G.C.; Laurent, S. Classification and basic properties of contrast agents for magnetic resonance imaging. *Contrast Media Mol. Imaging* **2009**, *4*, 1–23. [[CrossRef](#)]
18. Strijkers, G.J.; Mulder, W.J.M.; van Tilborg, G.A.F.; Nicolay, K. MRI contrast agents: Current status and future perspectives. *Anti-Cancer Agents Med. Chem.* **2007**, *7*, 291–305. [[CrossRef](#)]
19. Na, H.B.; Song, I.C.; Hyeon, T. Inorganic Nanoparticles for MRI Contrast Agents. *Adv. Mater.* **2009**, *21*, 2133–2148. [[CrossRef](#)]
20. Felton, C.; Karmakar, A.; Gartia, Y.; Ramidi, P.; Biris, A.S.; Ghosh, A. Magnetic nanoparticles as contrast agents in biomedical imaging: Recent advances in iron- and manganese-based magnetic nanoparticles. *Drug Metab. Rev.* **2014**, *46*, 142–154. [[CrossRef](#)]
21. Oliveira, I.S.; Hedgire, S.S.; Li, W.; Ganguli, S.; Prabhakar, A.M. Blood pool contrast agents for venous magnetic resonance imaging. *Cardiovasc. Diagn. Ther.* **2016**, *6*, 508–518. [[CrossRef](#)]
22. Thomsen, H.S.; Morcos, S.K.; Almén, T.; Bellin, M.-F.; Bertolotto, M.; Bongartz, G.; Clement, O.; Leander, P.; Heinz-Peer, G.; Reimer, P.; et al. Nephrogenic systemic fibrosis and gadolinium-based contrast media: Updated ESUR Contrast Medium Safety Committee guidelines. *Eur. Radiol.* **2013**, *23*, 307–318. [[CrossRef](#)] [[PubMed](#)]
23. Kattel, K.; Park, J.Y.; Chang, Y.; Kim, T.J.; Lee, G.H. Paramagnetic nanoparticle T₁ and T₂ MRI contrast agents. *Phys. Chem. Chem. Phys.* **2012**, *14*, 12687–12700.
24. Caro, C.; Paez-Muñoz, J.M.; Beltrán, A.M.; Leal, M.P.; García-Martín, M.L. PEGylated Terbium-Based Nanorods as Multimodal Bioimaging Contrast Agents. *ACS Appl. Nano Mater.* **2021**, *4*, 4199–4207. [[CrossRef](#)]
25. Hu, H.; Zhang, Y.; Shukla, S.; Gu, Y.; Yu, X.; Steinmetz, N.F. Dysprosium-Modified Tobacco Mosaic Virus Nanoparticles for Ultra-High-Field Magnetic Resonance and Near-Infrared Fluorescence Imaging of Prostate Cancer. *ACS Nano* **2017**, *11*, 9249–9258. [[CrossRef](#)]
26. Zheng, X.-Y.; Pellico, J.; Khrapitchev, A.A.; Sibson, N.R.; Davis, J.J. Dy-DOTA integrated mesoporous silica nanoparticles as promising ultrahigh field magnetic resonance imaging contrast agents. *Nanoscale* **2018**, *10*, 21041–21045. [[CrossRef](#)]
27. Norek, M.; Peters, J.A. MRI contrast agents based on dysprosium or holmium. *Prog. Nucl. Magn. Reson. Spectrosc.* **2011**, *59*, 64–82. [[CrossRef](#)]
28. Ni, D.; Zhang, J.; Bu, W.; Zhang, C.; Yao, Z.; Xing, H.; Wang, J.; Duan, F.; Liu, Y.; Fan, W.; et al. PEGylated NaHoF₄ nanoparticles as contrast agents for both X-ray computed tomography and ultra-high field magnetic resonance imaging. *Biomaterials* **2016**, *76*, 218–225. [[CrossRef](#)]
29. Thomsen, H.S. Nephrogenic Systemic Fibrosis: History and Epidemiology. *Radiol. Clin. N. Am.* **2009**, *47*, 827–831. [[CrossRef](#)]
30. Berstein, E.J.; Schmidt-Lauber, C.; Kay, J. Nephrogenic systemic fibrosis: A systemic fibrosing disease resulting from gadolinium exposure. *Best Pract. Res. Clin. Rheumatol.* **2012**, *26*, 489–503. [[CrossRef](#)]
31. Murata, N.; Murata, K.; Gonzalez-Cuyar, L.F.; Maravilla, K.R. Gadolinium tissue deposition in brain and bone. *Magn. Reson. Imaging* **2016**, *34*, 1359–1365. [[CrossRef](#)] [[PubMed](#)]
32. Khairinisa, M.A.; Ariyani, W.; Tsushima, Y.; Koibuchi, N. Effects of gadolinium deposits in the cerebellum: Reviewing the literature from in vitro laboratory studies to in vivo human investigations. *Int. J. Environ. Res. Public Health* **2021**, *18*, 7214. [[CrossRef](#)]
33. Abbaspour, N.; Hurrell, R.; Kelishadi, R. Review on iron and its importance for human health. *J. Res. Med. Sci.* **2014**, *19*, 164–174.
34. Wáng, Y.X.J.; Idée, J.-M. A comprehensive literatures update of clinical researches of superparamagnetic resonance iron oxide nanoparticles for magnetic resonance imaging. *Quant. Imaging Med. Surg.* **2017**, *7*, 88–122. [[CrossRef](#)]
35. Wang, Y.-X.J. Superparamagnetic iron oxide based MRI contrast agents: Current status of clinical application. *Quant. Imaging Med. Surg.* **2011**, *1*, 35–40.
36. Wang, Y.-X.J. Current status of superparamagnetic iron oxide contrast agents for liver magnetic resonance imaging. *World J. Gastroenterol.* **2015**, *21*, 13400–13402. [[CrossRef](#)]
37. Geppert, M.; Himly, M. Iron Oxide Nanoparticles in Bioimaging—An Immune Perspective. *Front. Immunol.* **2021**, *12*, 688927. [[CrossRef](#)]
38. Maurea, S.; Mainenti, P.P.; Tambasco, A.; Imbriaco, M.; Mollica, C.; Laccetti, E.; Camera, L.; Liuzzi, R.; Salvatore, M. Diagnostic accuracy of MR imaging to identify and characterize focal liver lesions: Comparison between gadolinium and superparamagnetic iron oxide contrast media. *Quant. Imaging Med. Surg.* **2014**, *4*, 181–189. [[PubMed](#)]

39. Doane, T.L.; Burda, C. The unique role of nanoparticles in nanomedicine: Imaging, drug delivery and therapy. *Chem. Soc. Rev.* **2012**, *41*, 2885–2911. [[CrossRef](#)] [[PubMed](#)]
40. Park, J.Y.; Baek, M.J.; Choi, E.S.; Woo, S.; Kim, J.H.; Kim, T.J.; Jung, J.C.; Chae, K.S.; Chang, Y.; Lee, G.H. Paramagnetic ultrasmall gadolinium oxide nanoparticles as advanced T₁ MRI contrast agent: Account for large longitudinal relaxivity, optimal particle diameter, and in vivo T₁ MR images. *ACS Nano* **2009**, *3*, 3663–3669. [[CrossRef](#)]
41. Ahrén, M.; Selegård, L.; Klasson, A.; Söderlind, F.; Abrikosova, N.; Skoglund, C.; Bengtsson, T.; Engström, M.; Käll, P.-O.; Uvdal, K. Synthesis and characterization of PEGylated Gd₂O₃ nanoparticles for MRI contrast enhancement. *Langmuir* **2010**, *26*, 5753–5762. [[CrossRef](#)]
42. Park, J.Y.; Choi, E.S.; Baek, M.J.; Lee, G.H.; Woo, S.; Chang, Y. Water-Soluble Ultra Small Paramagnetic or Superparamagnetic Metal Oxide Nanoparticles for Molecular MR Imaging. *Eur. J. Inorg. Chem.* **2009**, *2009*, 2477–2481. [[CrossRef](#)]
43. Ahmad, M.Y.; Ahmad, M.W.; Yue, H.; Ho, S.L.; Park, J.A.; Jung, K.-H.; Cha, H.; Marasini, S.; Ghazanfari, A.; Liu, S.; et al. In Vivo Positive Magnetic Resonance Imaging Applications of Poly(methyl vinyl ether-alt-maleic acid)-coated Ultra-small Paramagnetic Gadolinium Oxide Nanoparticles. *Molecules* **2020**, *25*, 1159. [[CrossRef](#)] [[PubMed](#)]
44. Bridot, J.-L.; Faure, A.-C.; Laurent, S.; Rivière, C.; Billotey, C.; Hiba, B.; Janier, M.; Jossierand, V.; Coll, J.-L.; Elst, L.V.; et al. Hybrid Gadolinium Oxide Nanoparticles: Multimodal Contrast Agents for In Vivo Imaging. *J. Am. Chem. Soc.* **2007**, *129*, 5076–5084. [[CrossRef](#)] [[PubMed](#)]
45. Hifumi, H.; Yamaoka, S.; Tanimoto, A.; Citterio, D.; Suzuki, K. Gadolinium-Based Hybrid Nanoparticles as a Positive MR Contrast Agent. *J. Am. Chem. Soc.* **2006**, *128*, 15090–15091. [[CrossRef](#)] [[PubMed](#)]
46. Estelrich, J.; Sánchez-Martín, M.J.; Busquets, M.A. Nanoparticles in magnetic resonance imaging: From simple to dual contrast agents. *Int. J. Nanomed.* **2015**, *10*, 1727–1741.
47. Bony, B.A.; Baeck, J.S.; Chang, Y.; Bae, J.E.; Chae, K.S.; Lee, G.H. A Highly Efficient New T₁ MRI Contrast Agent with r₂/r₁ ≈ 1.0: Mixed Cu(II)/Gd(III) Oxide Nanoparticle. *Bull. Korean Chem. Soc.* **2015**, *36*, 1203–1208.
48. Lauffer, R.B. Paramagnetic metal complexes as water proton relaxation agents for NMR imaging: Theory and design. *Chem. Rev.* **1987**, *87*, 901–927. [[CrossRef](#)]
49. Roch, A.; Muller, R.N.; Gillis, P. Theory of proton relaxation induced by superparamagnetic particles. *J. Chem. Phys.* **1999**, *110*, 5403–5411. [[CrossRef](#)]
50. Caravan, P.; Ellison, J.J.; McMurry, T.J.; Lauffer, R.B. Gadolinium(III) chelates as MRI contrast agents: Structure, dynamics, and applications. *Chem. Rev.* **1999**, *99*, 2293–2352. [[CrossRef](#)] [[PubMed](#)]
51. Greenwood, N.N.; Earnshaw, A. *Chemistry of the Elements*, 2nd ed.; Butterworth-Heinemann: Oxford, UK, 1998; p. 1243.
52. Wei, H.; Bruns, O.T.; Kaul, M.G.; Hansen, E.C.; Barch, M.; Wiśniowska, A.; Chen, O.; Chen, Y.; Li, N.; Okada, S.; et al. Exceedingly small iron oxide nanoparticles as positive MRI contrast agents. *Proc. Natl. Acad. Sci. USA* **2017**, *114*, 2325–2330. [[CrossRef](#)] [[PubMed](#)]
53. Tao, C.; Zheng, Q.; An, L.; He, M.; Lin, J.; Tian, Q.; Yang, S. T₁-Weight Magnetic Resonance Imaging Performances of Iron Oxide Nanoparticles Modified with a Natural Protein Macromolecule and an Artificial Macromolecule. *Nanomaterials* **2019**, *9*, 170. [[CrossRef](#)] [[PubMed](#)]
54. Besenhard, M.O.; Panariello, L.; Kiefer, C.; LaGrow, A.P.; Storozhuk, L.; Perton, F.; Begin, S.; Mertz, D.; Thanh, N.T.K.; Gavriilidis, A. Small iron oxide nanoparticles as MRI T₁ contrast agent: Scalable inexpensive water-based synthesis using a flow reactor. *Nanoscale* **2021**, *13*, 8795–8805. [[CrossRef](#)] [[PubMed](#)]
55. Tromsdorf, U.I.; Bruns, O.T.; Salmen, S.C.; Beisiegel, U.; Weller, H. A highly effective, nontoxic T₁ MR contrast agent based on ultrasmall PEGylated iron oxide nanoparticles. *Nano Lett.* **2009**, *9*, 4434–4440. [[CrossRef](#)] [[PubMed](#)]
56. Kim, B.H.; Lee, N.; Kim, H.; An, K.; Park, Y.I.; Choi, Y.; Shin, K.; Lee, Y.; Kwon, S.G.; Na, H.B.; et al. Large-scale synthesis of uniform and extremely small-sized iron oxide nanoparticles for high-resolution T₁ magnetic resonance imaging contrast agents. *J. Am. Chem. Soc.* **2011**, *133*, 12624–12631. [[CrossRef](#)] [[PubMed](#)]
57. Rui, Y.-P.; Liang, B.; Hu, F.; Xu, J.; Peng, Y.-F.; Yin, P.-H.; Duan, Y.; Zhang, C.; Gu, H. Ultra-large-scale production of ultrasmall superparamagnetic iron oxide nanoparticles for T₁-weighted MRI. *RSC Adv.* **2016**, *6*, 22575–22585. [[CrossRef](#)]
58. Luo, Y.; Yang, J.; Yan, Y.; Li, J.; Shen, M.; Zhang, G.; Mignani, S.; Shi, X. RGD-functionalized ultrasmall iron oxide nanoparticles for targeted T₁-weighted MR imaging of gliomas. *Nanoscale* **2015**, *7*, 14538–14546. [[CrossRef](#)]
59. Koenig, S.H.; Keller, K.E. Theory of 1/T₁ and 1/T₂ NMRD Profiles of Solutions of Magnetic Nanoparticles. *Magn. Reson. Med.* **1995**, *34*, 227–233. [[CrossRef](#)]
60. Zhang, W.; Liu, L.; Chen, H.; Hu, K.; Delahunty, I.; Gao, S.; Xie, J. Surface impact on nanoparticle-based magnetic resonance imaging contrast agents. *Theranostics* **2018**, *8*, 2521–2548. [[CrossRef](#)]
61. Kostevšek, N. A Review on the Optimal Design of Magnetic Nanoparticle-Based T₂ MRI Contrast Agents. *Magnetochemistry* **2020**, *6*, 11. [[CrossRef](#)]
62. Norek, M.; Kampert, E.; Zeitler, U.; Peters, J.A. Tuning of the size of Dy₂O₃ nanoparticles for optimal performance as an MRI contrast agent. *J. Am. Chem. Soc.* **2008**, *130*, 5335–5340. [[CrossRef](#)]
63. Norek, M.; Pereira, G.A.; Geraldès, C.F.G.C.; Denkova, A.; Zhou, W.; Peters, J.A. NMR transversal relaxivity of suspensions of lanthanide oxide nanoparticles. *J. Phys. Chem. C* **2007**, *111*, 10240–10246. [[CrossRef](#)]
64. Zhang, X.; Blasiak, B.; Merenco, A.J.; Trudel, S.; Tomanek, B.; van Veggel, F.C.J.M. Design and regulation of NaHoF₄ and NaDyF₄ nanoparticles for high field magnetic resonance imaging. *Chem. Mater.* **2016**, *28*, 3060–3072. [[CrossRef](#)]

65. Tegafaw, T.; Xu, W.; Ahmad, M.W.; Baeck, J.S.; Chang, Y.; Bae, J.E.; Chae, K.S.; Kim, T.J.; Lee, G.H. Dual-mode T₁ and T₂ magnetic resonance imaging contrast agent based on ultrasmall mixed gadolinium-dysprosium oxide nanoparticles: Synthesis, characterization, and in vivo application. *Nanotechnology* **2015**, *26*, 365102. [[CrossRef](#)]
66. Wang, Z.; Liu, J.; Li, T.; Liu, J.; Wang, B. Controlled synthesis of MnFe₂O₄ nanoparticles and Gd complex-based nanocomposites as tunable and enhanced T₁/T₂-weighted MRI contrast agents. *J. Mater. Chem. B* **2014**, *2*, 4748–4753. [[CrossRef](#)] [[PubMed](#)]
67. Huang, G.; Li, H.; Chen, J.; Zhao, Z.; Yang, L.; Chi, X.; Chen, Z.; Wang, X.; Gao, J. Tunable T₁ and T₂ contrast abilities of manganese-engineered iron oxide nanoparticles through size control. *Nanoscale* **2014**, *6*, 10404–10412. [[CrossRef](#)] [[PubMed](#)]
68. Im, G.H.; Kim, S.M.; Lee, D.-G.; Lee, W.J.; Lee, J.H.; Lee, I.S. Fe₃O₄/MnO hybrid nanocrystals as a dual contrast agent for both T₁- and T₂-weighted liver MRI. *Biomaterials* **2013**, *34*, 2069–2076. [[CrossRef](#)]
69. Yang, M.; Gao, L.; Liu, K.; Luo, C.; Wang, Y.; Yu, L.; Peng, H.; Zhang, W. Characterization of Fe₃O₄/SiO₂/Gd₂O(CO₃)₂ core/shell/shell nanoparticles as T₁ and T₂ dual mode MRI contrast agent. *Talanta* **2015**, *131*, 661–665. [[CrossRef](#)]
70. Shin, T.H.; Choi, J.S.; Yun, S.; Kim, I.S.; Song, H.T.; Kim, Y.; Park, K.I.; Cheon, J. T₁ and T₂ dual-mode MRI contrast agent for enhancing accuracy by engineered nanomaterials. *ACS Nano* **2014**, *8*, 3393–3401. [[CrossRef](#)]
71. Cheng, K.; Yang, M.; Zhang, R.; Qin, C.; Su, X.; Cheng, Z. Hybrid nanotrimers for dual T₁ and T₂-weighted magnetic resonance imaging. *ACS Nano* **2014**, *8*, 9884–9896. [[CrossRef](#)]
72. Tegafaw, T.; Xu, W.; Lee, S.H.; Chae, K.S.; Cha, H.; Chang, Y.; Lee, G.H. Ligand-size and ligand-chain hydrophilicity effects on the relaxometric properties of ultrasmall Gd₂O₃ nanoparticles. *AIP Adv.* **2016**, *6*, 065114. [[CrossRef](#)]
73. Miao, X.; Xu, W.; Cha, H.; Chang, Y.; Oh, I.T.; Chae, K.S.; Tegafaw, T.; Ho, S.L.; Kim, S.J.; Lee, G.H. Ultrasmall Gd₂O₃ nanoparticles surface-coated by polyacrylic acid (PAA) and their PAA-size dependent relaxometric properties. *Appl. Surf. Sci.* **2019**, *477*, 111–115. [[CrossRef](#)]
74. Joos, A.; Löwa, N.; Wiekhorst, F.; Gleich, B.; Haase, A. Size-dependent MR relaxivities of magnetic nanoparticles. *J. Magn. Magn. Mater.* **2017**, *427*, 122–126. [[CrossRef](#)]
75. York, J.N.; Albanese, C.; Rodriguez, O.; Le, Y.-C.; Ackun-Farmmer, M.; Keuren, E.V. The effects of particle shape and size on T₂ relaxation in magnetic resonance imaging. *J. Biomed. Nanotechnol.* **2014**, *10*, 3392–3396. [[CrossRef](#)] [[PubMed](#)]
76. Frangville, C.; Gallois, M.; Li, Y.; Nguyen, H.H.; Lauth-de Viguierie, N.; Talham, D.R.; Mingotaud, C.; Marty, J.-D. Hyperbranched polymer mediated size-controlled synthesis of gadolinium phosphate nanoparticles: Colloidal properties and particle size-dependence on MRI relaxivity. *Nanoscale* **2016**, *8*, 4252–4259. [[CrossRef](#)]
77. Yang, J.; Shan, P.; Zhao, Q.; Zhang, S.; Li, L.; Yang, X.; Yu, X.; Lu, Z.; Wang, Z.; Zhang, X. A design strategy of ultrasmall Gd₂O₃ nanoparticles for T₁ MRI with high performance. *New J. Chem.* **2021**, *45*, 7270–7277. [[CrossRef](#)]
78. Dai, Y.; Wu, C.; Wang, S.; Li, Q.; Zhang, M.; Li, J.; Xu, K. Comparative study on in vivo behavior of PEGylated gadolinium oxide nanoparticles and Magnevist as MRI contrast agent. *Nanomed. Nanotechnol. Biol. Med.* **2018**, *14*, 547–555. [[CrossRef](#)]
79. Wei, R.; Liu, K.; Zhang, K.; Fan, Y.; Lin, H.; Gao, J. Zwitterion-Coated Ultrasmall MnO Nanoparticles Enable Highly Sensitive T₁-Weighted Contrast-Enhanced Brain Imaging. *ACS Appl. Mater. Interfaces* **2022**, *14*, 3784–3791. [[CrossRef](#)]
80. Li, J.; Wu, C.; Hou, P.; Zhang, M.; Xu, K. One-pot preparation of hydrophilic manganese oxide nanoparticles as T₁ nano-contrast agent for molecular magnetic resonance imaging of renal carcinoma in vitro and in vivo. *Biosens. Bioelectron.* **2018**, *102*, 1–8. [[CrossRef](#)]
81. Xiao, J.; Tian, X.M.; Yang, C.; Liu, P.; Luo, N.Q.; Liang, Y.; Li, H.B.; Chen, D.H.; Wang, C.X.; Li, L.; et al. Ultrahigh relaxivity and safe probes of manganese oxide nanoparticles for in vivo imaging. *Sci. Rep.* **2013**, *3*, 3424. [[CrossRef](#)]
82. Zhao, Z.; Zhou, Z.; Bao, J.; Wang, Z.; Hu, J.; Chi, X.; Ni, K.; Wang, R.; Chen, X.; Chen, Z.; et al. Octapod iron oxide nanoparticles as high-performance T₂ contrast agents for magnetic resonance imaging. *Nat. Commun.* **2013**, *4*, 2266. [[CrossRef](#)] [[PubMed](#)]
83. Wang, Y.; Xu, C.; Chang, Y.; Zhao, L.; Zhang, K.; Zhao, Y.; Gao, F.; Gao, X. Ultrasmall Superparamagnetic Iron Oxide Nanoparticle for T₂-Weighted Magnetic Resonance Imaging. *ACS Appl. Mater. Interfaces* **2017**, *9*, 28959–28966. [[CrossRef](#)] [[PubMed](#)]
84. Leal, M.P.; Muñoz-Hernández, C.; Berry, C.C.; García-Martín, M.L. In vivo pharmacokinetics of T₂ contrast agents based on iron oxide nanoparticles: Optimization of blood circulation times. *RSC Adv.* **2015**, *5*, 76883–76891. [[CrossRef](#)]
85. Lee, N.; Choi, Y.; Lee, Y.; Park, M.; Moon, W.K.; Choi, S.H.; Hyeon, T. Water-dispersible ferrimagnetic iron oxide nanocubes with extremely high r₂ relaxivity for highly sensitive in vivo MRI of tumors. *Nano Lett.* **2012**, *12*, 3127–3131. [[CrossRef](#)]
86. Gueron, M. Nuclear relaxation in macromolecules by paramagnetic ions: A novel mechanism. *J. Magn. Reson.* **1975**, *19*, 58–66. [[CrossRef](#)]
87. Caravan, P.; Greenfield, M.T.; Bulte, J.W.M. Molecular factors that determine Curie spin relaxation in dysprosium complexes. *Magn. Reson. Med.* **2001**, *46*, 917–922. [[CrossRef](#)]
88. González-Mancebo, D.; Becerro, A.I.; Rojas, T.C.; García-Martín, M.L.; de la Fuente, J.M.; Ocaña, M. HoF₃ and DyF₃ Nanoparticles as Contrast Agents for High-Field Magnetic Resonance Imaging. *Part. Part. Syst. Character.* **2017**, *34*, 1700116. [[CrossRef](#)]
89. Kattel, K.; Park, J.Y.; Xu, W.; Kim, H.G.; Lee, E.J.; Bony, B.A.; Heo, W.C.; Jin, S.; Baeck, J.S.; Chang, Y.; et al. Paramagnetic dysprosium oxide nanoparticles and dysprosium hydroxide nanorods as T₂ MRI contrast agents. *Biomaterials* **2012**, *33*, 3254–3261. [[CrossRef](#)]
90. Yue, H.; Park, J.A.; Ho, S.L.; Ahmad, M.Y.; Cha, H.; Liu, S.; Tegafaw, T.; Marasini, S.; Ghazanfari, A.; Kim, S.; et al. New Class of Efficient T₂ Magnetic Resonance Imaging Contrast Agent: Carbon-Coated Paramagnetic Dysprosium Oxide Nanoparticles. *Pharmaceutics* **2020**, *13*, 312. [[CrossRef](#)]

91. Marasini, S.; Yue, H.; Ho, S.L.; Cha, H.; Park, J.A.; Jung, K.H.; Ghazanfari, A.; Ahmad, M.Y.; Liu, S.; Chae, K.S.; et al. A Novel Paramagnetic Nanoparticle T₂ Magnetic Resonance Imaging Contrast Agent with High Colloidal Stability: Polyacrylic Acid-Coated Ultrafine Dysprosium Oxide Nanoparticles. *Bull. Korean Chem. Soc.* **2020**, *41*, 829–836. [[CrossRef](#)]
92. Gómez-González, E.; Caro, C.; García-Martín, M.L.; Becerro, A.I.; Ocaña, M. Outstanding MRI contrast with dysprosium phosphate nanoparticles of tuneable size. *Nanoscale* **2022**, *14*, 11461–11470. [[CrossRef](#)]
93. Gómez-González, E.; Caro, C.; Martínez-Gutierrez, D.; García-Martín, M.L.; Ocaña, M.; Becerro, A.I. Holmium phosphate nanoparticles as negative contrast agents for high-field magnetic resonance imaging: Synthesis, magnetic relaxivity study and in vivo evaluation. *J. Colloid Interface Sci.* **2021**, *587*, 131–140. [[CrossRef](#)]
94. Atabaev, T.S.; Shin, Y.C.; Song, S.-J.; Han, D.-W.; Hong, N.H. Toxicity and T₂-Weighted Magnetic Resonance Imaging Potentials of Holmium Oxide Nanoparticles. *Nanomaterials* **2017**, *7*, 216. [[CrossRef](#)]
95. Zhang, T.; Deng, M.; Zhang, L.; Liu, Z.; Liu, Y.; Song, S.; Gong, T.; Yuan, Q. Facile Synthesis of Holmium-Based Nanoparticles as a CT and MRI Dual-Modal Imaging for Cancer Diagnosis. *Front. Oncol.* **2021**, *11*, 741383. [[CrossRef](#)]
96. Marasini, S.; Yue, H.; Ho, S.L.; Park, J.A.; Kim, S.; Jung, K.-H.; Cha, H.; Liu, S.; Tegafaw, T.; Ahmad, M.Y.; et al. Synthesis, Characterizations, and 9.4 Tesla T₂ MR Images of Polyacrylic Acid-Coated Terbium(III) and Holmium(III) Oxide Nanoparticles. *Nanomaterials* **2021**, *11*, 1355. [[CrossRef](#)]
97. Liu, S.; Yue, H.; Ho, S.L.; Kim, S.; Park, J.A.; Tegafaw, T.; Ahmad, M.Y.; Kim, S.; Saidi, A.K.A.A.; Zhao, D.; et al. Polyethylenimine-Coated Ultrasmall Holmium Oxide Nanoparticles: Synthesis, Characterization, Cytotoxicities, and Water Proton Spin Relaxivities. *Nanomaterials* **2022**, *12*, 1588. [[CrossRef](#)] [[PubMed](#)]
98. Liu, S.; Tegafaw, T.; Yue, H.; Ho, S.L.; Kim, S.; Park, J.A.; Baek, A.; Ahmad, M.Y.; Yang, S.H.; Hwang, D.W.; et al. Paramagnetic ultrasmall Ho₂O₃ and Tm₂O₃ nanoparticles: Characterization of r₂ values and in vivo T₂ MR images at a 3.0 T MR field. *Mater. Adv.* **2022**, *3*, 5857–5870. [[CrossRef](#)]
99. Zheng, X.; Wang, Y.; Sun, L.; Chen, N.; Li, L.; Shi, S.; Malaisamy, S.; Yan, C. TbF₃ nanoparticles as dual-mode contrast agents for ultrahigh field magnetic resonance imaging and X-ray computed tomography. *Nano Res.* **2016**, *9*, 1135–1147. [[CrossRef](#)]
100. Marasini, S.; Yue, H.; Ho, S.L.; Jung, K.H.; Park, J.A.; Cha, H.; Ghazanfari, A.; Ahmad, M.Y.; Liu, S.; Jang, Y.J.; et al. D-Glucuronic Acid-Coated Ultrasmall Paramagnetic Ln₂O₃ (Ln = Tb, Dy, and Ho) Nanoparticles: Magnetic Properties, Water Proton Relaxivities, and Fluorescence Properties. *Eur. J. Inorg. Chem.* **2019**, *2019*, 3832–3839. [[CrossRef](#)]
101. Zhou, Z.; Zhao, Z.; Zhang, H.; Wang, Z.; Chen, X.; Wang, R.; Chen, Z.; Gao, J. Interplay between longitudinal and transverse contrasts in Fe₃O₄ nanoplates with (111) exposed surfaces. *ACS Nano* **2014**, *8*, 7976–7985. [[CrossRef](#)]
102. Wang, G.; Zhang, X.; Skallberg, A.; Liu, Y.; Hu, Z.; Mei, X.; Uvdal, K. One-step synthesis of water-dispersible ultra-small Fe₃O₄ nanoparticles as contrast agents for T₁ and T₂ magnetic resonance imaging. *Nanoscale* **2014**, *6*, 2953–2963. [[CrossRef](#)]
103. Si, G.; Hapuarachchige, S.; Artemov, D. Ultrasmall Superparamagnetic Iron Oxide Nanoparticles as Nanocarriers for Magnetic Resonance Imaging: Development and In Vivo Characterization. *ACS Appl. Nano Mater.* **2022**, *5*, 9625–9632. [[CrossRef](#)] [[PubMed](#)]
104. Li, Z.; Yi, P.W.; Sun, Q.; Lei, H.; Zhao, H.L.; Zhu, Z.H.; Smith, S.C.; Lan, M.B.; Lu, G.Q. Ultrasmall Water-Soluble and Biocompatible Magnetic Iron Oxide Nanoparticles as Positive and Negative Dual Contrast Agents. *Adv. Funct. Mater.* **2012**, *22*, 2387–2393. [[CrossRef](#)]
105. Sharma, V.K.; Alipour, A.; Soran-Erdem, Z.; Aykut, Z.G.; Demir, H.V. Highly monodisperse low-magnetization magnetite nanocubes as simultaneous T₁-T₂ MRI contrast agents. *Nanoscale* **2015**, *7*, 10519–10526. [[CrossRef](#)] [[PubMed](#)]
106. Thapa, B.; Diaz-Diestra, D.; Santiago-Medina, C.; Kumar, N.; Tu, K.; Beltran-Huarac, J.; Jadwisienczak, W.M.; Weiner, B.R.; Morell, G. T₁- and T₂-weighted Magnetic Resonance Dual Contrast by Single Core Truncated Cubic Iron Oxide Nanoparticles with Abrupt Cellular Internalization and Immune Evasion. *ACS Appl. Bio. Mater.* **2018**, *1*, 79–89. [[CrossRef](#)]
107. Li, J.; Li, X.; Gong, S.; Zhang, C.; Qian, C.; Qiao, H.; Sun, M. Dual-Mode Avocado-like All-Iron Nanoplatfor for Enhanced T₁/T₂ MRI-Guided Cancer Theranostic Therapy. *Nano Lett.* **2020**, *20*, 4842–4849. [[CrossRef](#)] [[PubMed](#)]
108. Hou, X.; Yang, X.; Xu, Y.; Lin, J.; Zhang, F.; Duan, X.; Liu, S.; Liu, J.; Shen, J.; Shuai, X.; et al. Manganese-doped mesoporous polydopamine nanoagent for T₁-T₂ magnetic resonance imaging and tumor therapy. *Nano Res.* **2023**, *16*, 2991–3003. [[CrossRef](#)]
109. Miao, C.; Hu, F.; Rui, Y.; Duan, Y.; Gu, H. A T₁/T₂ dual functional iron oxide MRI contrast agent with super stability and low hypersensitivity benefited by ultrahigh carboxyl group density. *J. Mater. Chem. B* **2019**, *7*, 2081–2091. [[CrossRef](#)] [[PubMed](#)]
110. Mekuria, S.L.; Debele, T.A.; Tsai, H.-C. Encapsulation of Gadolinium Oxide Nanoparticle (Gd₂O₃) Contrasting Agents in PAMAM Dendrimer Templates for Enhanced Magnetic Resonance Imaging in Vivo. *ACS Appl. Mater. Interfaces* **2017**, *9*, 6782–6795. [[CrossRef](#)]
111. Marasini, S.; Yue, H.; Ghazanfari, A.; Ho, S.L.; Park, J.A.; Kim, S.; Cha, H.; Liu, S.; Tegafaw, T.; Ahmad, M.Y.; et al. Polyaspartic Acid-Coated Paramagnetic Gadolinium Oxide Nanoparticles as a Dual-Modal T₁ and T₂ Magnetic Resonance Imaging Contrast Agent. *Appl. Sci.* **2021**, *11*, 8222. [[CrossRef](#)]
112. Niu, D.; Luo, X.; Li, Y.; Liu, X.; Wang, X.; Shi, J. Manganese-loaded dual-mesoporous silica spheres for efficient T₁- and T₂-weighted dual mode magnetic resonance imaging. *ACS Appl. Mater. Interfaces* **2013**, *5*, 9942–9948. [[CrossRef](#)]
113. Alromi, D.A.; Madani, S.Y.; Seifalian, A. Emerging application of magnetic nanoparticles for diagnosis and treatment of cancer. *Polymers* **2021**, *13*, 4146. [[CrossRef](#)] [[PubMed](#)]
114. Ahmad, M.Y.; Yue, H.; Tegafaw, T.; Liu, S.; Ho, S.L.; Lee, G.H.; Nam, S.-W.; Chang, Y. Functionalized lanthanide oxide nanoparticles for tumor targeting, medical imaging, and therapy. *Pharmaceutics* **2021**, *13*, 1890. [[CrossRef](#)] [[PubMed](#)]

115. Longmire, M.; Choyke, P.L.; Kobayashi, H. Clearance properties of nano-sized particles and molecules as imaging agents: Considerations and caveats. *Nanomedicine* **2008**, *3*, 703–717. [[CrossRef](#)]
116. Choi, H.S.; Liu, W.; Misra, P.; Tanaka, E.; Zimmer, J.P.; Ipe, B.I.; Bawendi, M.G.; Frangioni, J.V. Renal clearance of nanoparticles. *Nat. Biotechnol.* **2007**, *25*, 1165–1170. [[CrossRef](#)]
117. Xu, J.; Peng, C.; Yu, M.; Zheng, J. Renal clearable noble metal nanoparticles: Photoluminescence, elimination, and biomedical applications. *WIREs Nanomed. Nanobiotechnol.* **2017**, *9*, e1453. [[CrossRef](#)] [[PubMed](#)]

Disclaimer/Publisher’s Note: The statements, opinions and data contained in all publications are solely those of the individual author(s) and contributor(s) and not of MDPI and/or the editor(s). MDPI and/or the editor(s) disclaim responsibility for any injury to people or property resulting from any ideas, methods, instructions or products referred to in the content.